Mixing, fluid Infiltration, Leaching, and Deformation (MILD) processes on the slab-mantle wedge interface at high *T* and *P* conditions: Records from the Dalrymple Amphibolite, Philippines

Gabriel Theophilus V. VALERA[1,*], Tetsuo KAWAKAMI[1], Betchaida D. PAYOT[2]

[1]Department of Geology and Mineralogy, Graduate School of Science, Kyoto University, Kitashirakawa-Oiwake-cho, Sakyo-ku, Kyoto 606-8502, Japan

[2] National Institute of Geological Sciences, University of the Philippines, Diliman, Quezon City 1101, Philippines

*corresponding author: gtv.valera@gmail.com

Abstract

The whole rock compositions of the blocks and the surrounding matrix of the Dalrymple Amphibolite are investigated in this study to determine the protolith of the blocks and the effect of mechanical mixing and fluid infiltration in the matrix of this fossil slab-mantle wedge interface. The major and trace element contents of the metamafic blocks indicate their mid-oceanic ridge basalt origin similar to the mafic lavas of the crustal section of central Palawan Ophiolite. Similarities in their rare earth and trace element patterns indicate the genetic relationship between the mafic lavas of the Palawan Ophiolite and the metamafic blocks of the Dalrymple Amphibolite. This confirms that the metamafic blocks represent the basalt to gabbro section of the oceanic lithosphere of the subducting slab.

The matrix surrounding the blocks exhibit highly variable phase assemblages. In order to determine its petrogenesis, we distinguished groups of components/elements which behave similarly (Group 1 TiO_2, Al_2O_3, Zr, Th and the light rare earth elements; Group 2 Cr, Ni and MgO) based on geostatistical (correlation coefficient) analyses. These groups indicate mixing of metasedimentary (Group 1) and metamafic (Group 2) end-members to form the matrix. The mixing proportions of the end-members were estimated by employing regression analysis wherein the measured concentration of fluid immobile elements (Cr, Ni, Zr, TiO_2 and Al_2O_3) in the matrix samples were fitted against a modelled concentration by changing the end-member and their relative proportions. The end-members and mixing ratio with the highest regression value (r^2) was selected to obtain the modelled composition of the matrix. The modelled and the measured matrix compositions were then used as the original (unmetasomatized) rock and the altered rock respectively in the isocon analysis, assuming that TiO_2, Al_2O_3, Cr, Nd, Zr, and Hf are immobile. This assumption is supported by the prevalence of kyanite, ilmenite and zircon in the matrix mineral assemblage.

This procedural workflow helped distinguish end-member components, estimate their mixing ratios, and determine the effects of infiltrating fluids. In particular, the whole rock composition of the matrix was controlled by mixing of a subordinate amount of metamafic blocks in a metasedimentary-dominated shear

zone. This is supported by the Cr-Nb content of rutile grains included in the matrix samples which indicate mixed metamafic and metapelitic signatures. The metamafic-metasedimentary dominated matrix in the Dalrymple Amphibolite contrasts with other high-pressure/temperature (*P/T*) type metamorphic terranes which are dominated by low *T* minerals (serpentine, Mg-chlorite, and talc) derived from an ultramafic end-member, and could be reflective of conditions in warmer subduction zones. Mass balance calculations further revealed that an early fluid infiltration event likely occurred following the mixing process. This preferentially leached out elements which are either fluid-mobile (e.g. CaO and SiO_2) or are not incorporated into the growing minerals in the matrix. The strong control of mineral assemblage of the matrix in its chemistry is exhibited by a number of samples which showed variable degrees of losses and gains in elements traditionally interpreted to be fluid immobile (e.g. heavy rare earth elements and Y). A later hydration event linked to retrograde metamorphic stage imprinted gains of K_2O, Rb, and Ba in the matrix samples with the growth of replacement minerals (e.g. muscovite on kyanite). This later fluid infiltration event possibly masked the original loss of these fluid-mobile elements in the matrix samples during the earlier fluid-rock interaction.

Keywords: Dalrymple Amphibolite, mechanical mixing, fluid infiltration, leaching, slab-mantle wedge interface

1. Introduction

The slab-mantle wedge interface separates the subducting oceanic lithosphere from the overlying mantle wedge in subduction zones. This region, also referred to as the subduction channel (e.g. Guillot et al., 2009; Bebout and Penniston-Dorland, 2016) or subduction plate interface (e.g. Agard et al., 2018), serves as the locus of interaction between crustal and mantle lithologies, and where mafic and sedimentary components from the subducting slab are recycled for utilization in the subduction factory (e.g. Tatsumi, 2005). Thought to represent paleo slab-mantle wedge interfaces, high-pressure mélange zones, provide a picture of fluid-rich shear zones of tens to hundred meters-wide, composed of metamafic, metasedimentary, and metaultramafic blocks surrounded by a matrix of hybrid composition (e.g. Bebout and Penniston-Dorland, 2016). These deformation zones also serve as pathways for migrating fluids derived from the dehydrating slab. Whole rock geochemical data from arc lavas and experimental analyses suggest the important role that this interface plays in controlling the overall arc magma chemistry (e.g. Nielsen and Marschall, 2017; Codillo et al., 2018).

The complex interplay between deformation, mechanical mixing of end-member components (sediments, mafic crust and mantle materials), and fluid advection are reflected in the highly variable phase assemblage and whole-rock composition of the matrix material surrounding the blocks in different slab-mantle wedge interface exposures and even within a single locality (e.g. Dalrymple Amphibolite; Table 1). The juxtaposition of rocks with disparate composition for extended periods can further lead to diffusive material transfer at centimeter to meter scales among blocks and between block-matrix pairs (e.g. Bebout and Barton, 2002). Most studies on the petrological evolution of the slab-mantle wedge interface are focused on the pressure-temperature-deformation (*P-T-D*) evolution and petrogenesis of the blocks in these terranes primarily due to the relatively poorer preservation state of the softer matrix material in most localities and/or the extensive fluid flux passing through these sheared domains causing either leaching and/or retrograde overprint (Marschall and Schumacher, 2012). The change in paleogeothermal gradient of this interface as subduction progresses is another consideration when studying these terranes (Agard et

al., 2018). The petrological characteristics of the lithologies comprising the slab-mantle wedge interface during subduction initiation and in mature arcs have largely been constrained through studies of metamorphic soles beneath ophiolites and exhumed high-*P/T* type metamorphic terranes, respectively. Localities preserving the petrological characteristics of both blocks and matrix, as well as prograde to peak *P-T* conditions comparable to the slab-mantle wedge interface as it transitions from a young and hot margin to a mature arc are equally important albeit less common. One such locality with an intermediate paleogeothermal gradient is the Dalrymple Amphibolite in Palawan Island, Philippines (Valera et al., 2021; Fig. 1a,b).

In this study, whole rock geochemical data of metamafic-metasedimentary blocks and sheared matrix samples are used to determine the petrogenesis of the Dalrymple Amphibolite. Major oxide and trace element contents of the metamafic blocks revealed their mid-oceanic ridge basalt (MORB) origin and genetic relation with the mafic oceanic crust of the central Palawan Ophiolite (CPO). The petrogenesis of the matrix, on the other hand, records the combined effects of mechanical mixing and multiple stages of fluid infiltration. In addition to conventional binary plots and trace element spidergrams, the compounding effects of mechanical and fluid-related processes on the matrix are distinguished by employing statistical (i.e. correlation coefficient) and isocon analysis. Mineral chemistry data are also utilized in this work although a more complete assessment is available in Valera et al. (2021) which used the same samples. Mineral abbreviations are after Whitney and Evans (2010) except for Ca-amphibole (Camp).

2. Geological background

Palawan Island in western Philippines consist of tectonically juxtaposed continental and oceanic terranes. The northern segment of the island, referred to as the North Palawan Continental Terrane (NPCT), is composed of Paleozoic to Eocene flysch-type turbiditic deposits (Fig. 1a). This microcontinental block drifted from the Southeast Asian continental margin during the Eocene to Oligocene which led to the opening of the South China Sea (SCS) basin in its northwestern margin (Fig. 1b). The tectonic shortening

104 is then thought to have induced subduction along a preexisting spreading center of the marginal basin in
105 its southeastern margin, typically referred to as the proto-South China Sea (e.g. Encarnacion et al., 1995;
106 Yumul et al., 2020; Dycoco et al., 2021). Closing of the proto-SCS subsequently led to the collision
107 between the NPCT and the nascent arc now exposed as the Palawan Ophiolite (Fig. 1b).

108 The Palawan Ophiolite is a Tethyan-type ophiolite exposed in central and southern segments of
109 Palawan Island. Slivers of this fossil oceanic lithosphere comprise the South Palawan Terrane (SPT) and
110 are thrusted on top of the NPCT lithologies. Based on systematic differences in petrological signatures
111 and tectonic setting of formation, recent works distinguish the Late Eocene to Early Oligocene central
112 Palawan Ophiolite (CPO) and the Cretaceous southern Palawan Ophiolite (SPO; Labis et al., 2020;
113 Dycoco et al., 2021). The Dalrymple Amphibolite is only found at the base of the hanging wall, below the
114 residual peridotites of the CPO (Fig. 1b,c).

115 The Dalrymple Amphibolite is a high-grade metamorphic sequence with block-in-matrix fabric. It
116 is predominantly composed of metamafic blocks and minor metasedimentary blocks surrounded by a
117 sheared matrix. The matrix exhibits variable mineralogy with some samples consisting of a mafic phase
118 assemblage (e.g. Ca-amphibole + garnet + kyanite + ilmenite) and others derived from a metasedimentary
119 protolith and are composed of kyanite + biotite + ilmenite ± garnet. Both the block and matrix record an
120 intermediate paleogeothermal gradient with similar peak *P-T* conditions of ~700 °C and 13 kbar (Fig. 1c;
121 Valera et al., 2021). Its block-in-matrix occurrence and cooler paleogeothermal gradients contrast with
122 typical metamorphic soles which consist of relatively coherent sheets with inverted thermal gradients of
123 >20 °C/km (e.g. Soret et al., 2017). The predominance of Ca-amphibole and kyanite in the matrix of the
124 Dalrymple Amphibolite is also distinct from other localities with cooler paleogeothermal gradients (4–
125 10 °C/km). The matrix of these localities are typically dominated by ultramafic-derived components
126 resulting to a phase assemblage dominated by phyllosilicates such as talc, serpentine and chlorite (Fig. 1b;
127 e.g. Bebout, 2013).

The mafic crust of the central Palawan Ophiolite (CPO) consists of basaltic pillow lavas, isotropic and layered gabbros and ultramafic cumulates. Petrological investigation of the mafic lavas and intrusives revealed a MORB (Gibaga et al., 2020) to transitional island arc basalt affinity (e.g. Keenan et al., 2016; Dycoco et al., 2021). Exposures of the mantle section of the ophiolite are found thrusted on top of the Dalrymple Amphibolite in Ulugan Bay (Valera et al., 2021). It is predominantly composed of moderately serpentinized interlayers of harzburgite and dunite. Late stage mafic dikes with distinct bake-and-chill margins crosscut the ophiolite sequence, from the metamorphic sole to the crustal section. The dikes exhibit similar tholeiitic basalt geochemical signature as the mafic crust of the ophiolite (Dycoco et al., 2021).

3. *P-T-D* history of the Dalrymple Amphibolite

The Dalrymple Amphibolite is a thin mélange complex (~50–200 m across) exposed primarily in Ulugan Bay in the localities of Botoon (Fig. 2a–f), Nanad (Fig. 2g–k) and Dalrymple points. Earlier works on the Dalrymple Amphibolite considered it as a typical metamorphic sole related to the Palawan Ophiolite based on its proximity and limited occurrence. Encarnacion et al. (1995) constrained peak *T* conditions of 700–760 °C at a minimum *P* of 9 kbar and attributed the mélange-like appearance to a later, 'cold' deformation event although *P-T* estimation for this deformation event is lacking. Valera et al. (2021) reevaluated the *P-T-D* history for the Dalrymple Amphibolite by constraining the *P-T* conditions for the metamafic blocks and the surrounding matrix. This *P-T-D* history (Fig. 1c) is adopted here and summarized below based on Valera et al. (2021).

The Dalrymple Amphibolite is composed of metamafic and minor metasedimentary blocks surrounded by a highly sheared matrix (Fig. 2). The metamafic blocks are amphibolite with variable amounts of garnet (i.e. Grt amphibolite; Fig. 2b–f) and epidote (i.e. Ep amphibolite). Deformed metamafic blocks in Nanad are highly sheared (Fig. 2h–i) and indicate a top to the NW sense of shear indicating the thrusting of the ultramafic section of the ophiolite on top of the amphibolite mélange sequence (cf. Fig. 3b of Valera et al., 2021). A brief description of the petrographic and mineral chemical characteristics of the

blocks and matrix samples are given in the sample description section. Since the samples used in this work are the same as those described in Valera et al. (2021), the reader is referred to the previous study for a more detailed description on the petrography and mineral chemistry of the metamafic blocks and the matrix samples. The paragenesis of the block and matrix of the Dalrymple Amphibolite is summarized in Fig. 3 while Table 1 lists the phase assemblage and mode of occurrence of the samples used (Valera et al., 2021). Earlier studies on the geochemical characteristics of the metamafic blocks suggest a mid-oceanic ridge basalt protolith similar to the mafic crust of the CPO (e.g. Keenan et al., 2016). This evidence supports the recent tectonic model of spreading center-turned-subduction zone for the CPO (e.g. Dycoco et al., 2021). According to this model, the Dalrymple Amphibolite represent the subducted equivalent of the same oceanic lithosphere now emplaced as the CPO (Fig. 1b). Compared to the metamafic blocks, no studies have been conducted on the petrogenesis of the metasedimentary blocks and the sheared matrix of the sequence. The metasedimentary blocks sampled in this study include Ep-Bt-Ms schist (D215-7), Camp-Ky-Qz schist (B214-26), Ky-Ilm-Grt quartzite (N215-4) and a metacarbonate (B214-7C).

Based on Valera et al. (2021), the *P-T-D* history of the Dalrymple Amphibolite was subdivided into the *P-T* conditions preserved in the block (Stage 1) and the matrix (Stage 2; Fig. 3). The growth of replacement minerals affecting both block and matrix samples are assigned Stage 3. The Zr-in-rutile geothermometry, following the methods of Tomkins et al. (2007) and quartz-in-garnet Raman geobarometry (e.g. Angel et al., 2017) applied to respective inclusions in the core and rim of garnet porphyroblasts of a Grt amphibolite block (B214-21) revealed the conditions for the prograde metamorphism of the metamafic blocks. The earliest stage of metamorphism (Stage 1) was subdivided as the Grt core assemblage (Stage 1a = ~625 °C, 11.5 kbar) and the garnet rim and matrix assemblage (Stage 1b = 700 °C, 13 kbar; Figs. 1c and 3; Valera et al., 2021). In Valera et al. (2021), the Ep amphibolite and amphibolite blocks preserve comparable peak metamorphic conditions constrained by Zr-in-rutile geothermometry (Tomkins et al., 2007) and the TZARS geobarometer based on the reaction 3 An + 2 Czo + Rt + Qz = 3 An + Ttn + H_2O (Kapp et al., 2009).

178 The matrix (Stage 2) surrounding the blocks are typically highly-sheared and exhibit variable
179 mineralogy but always include ilmenite and kyanite, with some samples containing variable amounts of
180 hornblende, biotite, quartz, and garnet (Table 1). The *P-T* history of the matrix and the deformation events
181 related to the transformation of the slab-mantle wedge interface into a mélange complex is grouped as
182 Stage 2 (Valera et al., 2021). In Botoon and Nanad, two generations of matrix formation (matrix2a and
183 2b) are identified (Figs. 2,3). Both matrix2a and 2b are defined by the same mineral assemblage but
184 distinguished by cross-cutting pervasive foliation directions and by lenses of matrix2a found in matrix2b
185 (Valera et al., 2021).

186 Geothermobarometry of a matrix2a sample (B214-14) constrained similar peak metamorphic
187 conditions (~700 °C, 13 kbar) as the metamafic blocks (Valera et al., 2021). This similarity in peak *P-T*
188 conditions was confirmed by pseudosection modelling and suggests that matrix forming processes (i.e.
189 deformation, mixing, and fluid-infiltration) occurred as the whole mélange sequence was being subducted
190 at depth (Valera et al., 2021). This is further supported by the 10-fold increase in the Nb content of rutile
191 grains included in the garnet rim of an amphibolite block (Stage 1b) indicating the start of the mafic-
192 sedimentary mixing during prograde metamorphism (Valera et al., 2021). Several generations of quartz,
193 quartz-kyanite, and epidote veins cross-cut the block and the matrix of the sequence, implying extensive
194 fluid activity throughout its *P-T-D* history.

195 Based on its block-in-matrix occurrence and the cooler paleogeothermal gradient (~16 °C/km)
196 preserved in the Dalrymple Amphibolite, the mélange is suggested to correspond to the slab-mantle wedge
197 interface of a young subduction complex already transitioning from the much warmer conditions of
198 subduction initiation (Valera et al., 2021). The relatively high *T/P* conditions for the Dalrymple
199 Amphibolite is attributed to the residual heat of the overlying mantle peridotites during early subduction
200 (Valera et al., 2021). The blocks and surrounding matrix were then affected by migrating fluids during its
201 retrograde metamorphism with maximum *T* and *P* conditions of ~600 °C, 8 kbar. This event promoted by
202 Stage 3 deformation (D3 in Fig. 3), led to the formation of replacement minerals such as chlorite (Chl3),

biotite (Bt3), actinolite (Camp3) and epidote (Ep3) at the expense of earlier-formed minerals in the blocks and matrix samples such as garnet (Grt1/Grt2), amphibole (Camp1/Camp2) and biotite (Bt1/Bt2; Valera et al., 2021). The matrix samples used in this study have variable degrees of Stage 3 imprinting. This allowed us to determine the progressive effect of fluid-related mass-transfer even as the metamorphic sequence was being exhumed.

4. Material and methods

Mineral chemistry analysis of rock-forming minerals and X-ray elemental mapping were conducted using a JEOL JXA-8105 electron probe microanalyzer. Analytical conditions for quantitative analyses were 15.0 kV acceleration voltage, 10 nA beam current, and 3 μm beam diameter. The counting time for the peak and backgrounds were 30 s and 15 s for Cl, 60 s and 30 s for F, and 10 s and 5 s for other elements. Natural and synthetic minerals were used as standards and ZAF correction was applied. Estimating Fe^{3+} in garnet and Ca-amphibole is after Droop (1987) and Schumacher (1991). Analytical conditions for determining trace element (Nb, Zr, and Cr) concentration of rutile followed that of Zack et al. (2004). Acceleration voltage used was 20.0 kV, 120 nA probe current and a probe diameter of 5 μm to determine both major and trace element concentration of the rutile grains. Elemental mapping was conducted using an acceleration voltage of 15.0 kV, probe current of 600-800 nA and a dwell time of 60-80 msec, with a beam diameter of 3–5 μm. These analyses were done at the Department of Geology and Mineralogy, Kyoto University.

Nineteen (19) metamafic blocks, four (4) metasedimentary blocks, and twelve (12) matrix samples, four of which contain both matrix2a and 2b were analyzed for whole rock major and trace element concentration (Table 1). Major and trace element data for blocks and matrix samples are given in Tables 2 and 3, respectively. The samples were selected to represent the variable mineralogy and degree of Stage 3 imprint on the blocks and the matrix. The samples were powdered in a tungsten-carbide mill at Kyoto University. Whole rock geochemical analyses were performed at Bureau Veritas, Perth, Australia. Major-

element concentrations were obtained by fused glass bead X-ray fluorescence (XRF) analysis while trace element data was obtained by laser ablation inductively coupled mass spectrometry (LA-ICPMS) of the same glass beads. Loss on ignition for the metamafic blocks are low (0.4–2.6%) while those of the matrix (1.38–4.72%) and metasedimentary blocks (1.1–13.49%) are generally higher. Analytical precision, i.e. relative standard deviation (RSD), based on replicate sample analysis done after every batch of ten samples, was within 1% for major oxides and 10% for trace elements. Accuracy based on standards is within 0.5% for major oxides except K_2O (1.89%) and within 7% for trace elements. Accuracy computation was done based on the reference materials EuroNorm 782-1 for major oxides and NSC DC 86308 Zirconium Ore for trace elements. The secondary standard SDSYB was also analyzed together with the samples. Comparing our results with those of Nakashima et al. (2000) and Shimoda et al. (2004) yielded RSD values of within 1% for most major elements except MgO (3.97%) and K_2O (5.88%), and better than 5% for most trace elements except Rb (17.71%), Pb (14.29%), Nd (23.53%) and Yb (14.37%). High RSD values for Pb, Nd, Yb (>10 ppm) and Rb (~30 ppm) are ascribed to low concentration of these elements in SDSYB.

5. Sample description

5.1 Petrographic and mineral chemical characteristics of the blocks

Detailed description of the petrographic and mineral chemistry of the metamafic block samples used in this study are available in Valera et al. (2021) such that only a general description follows. The metamafic blocks are amphibolites composed of Camp+Qz with varying amounts of garnet, epidote (clinozoisite) and plagioclase. Accessory minerals in the metamafic blocks are biotite, rutile, ilmenite, and zircon. The garnet porphyroblasts in the Grt amphibolite blocks preserve prograde zonation. This is marked by decreasing spessartine content and increasing Mg# [= $Mg/(Mg+Fe^{2+})$] from core (e.g. B214-21 = $Alm_{46–51}Prp_{10–19}Grs_{15–20}Sps_{15–25}$) to rim (= $Alm_{38–41}Prp_{30–35}Grs_{13–15}Sps_{13–17}$; cf. Valera et al., 2021). At the core of some garnet porphyroblasts are multiphase solid inclusions which consist of lower-T

assemblage (Chl+Ep+Qz+Grt+Rt+Ilm). The rim of the garnet porphyroblasts are in textural equilibrium with the surrounding matrix of Ca-amphibole and epidote (Fig. 2d–f; Valera et al., 2021).

Ca-amphibole in the amphibolites are classified as hornblende (Leake et al., 1997). They range from ferrotschermakite to tschermakite with minor magnesiohornblende in the Grt amphibolite blocks. Those in the amphibolites and Ep amphibolites range from tschermakite to magnesiohornblende with slightly lower total Al content and higher Si and Mg# than the Grt amphibolite. Replacement of hornblende in the blocks by actinolite are common especially in Ep amphibolites (Valera et al., 2021). Epidote in the metamafic blocks are more common in the amphibolite and Ep amphibolite. They generally have higher pistacite (Ps) component at the core (= Ps20–29) compared to the rim (= Ps22–27).

Plagioclase are found only in the metamafic blocks in Dalrymple point. Most plagioclases are Ca-poor: $An_{1\text{-}15}$ in Ep amphibolites, $An_{2\text{-}17}$ in amphibolites and $An_{10–18}$ in Grt amphibolites. Some Ep amphibolite (D113-8: $An_{16–27}$) and Grt amphibolite (D113-15: $An_{15–24}$) blocks however have higher anorthite content (Valera et al., 2021). These blocks represent a gabbroic protolith as discussed below. Rutile in the metamafic blocks generally have low Nb content (<2000 ppm). Rutile grains included in the rim of the garnet porphyroblasts and in the matrix of the Grt amphibolite blocks B214-21 however shows a ten-fold increase in Nb concentration (720–5606 ppm) compared to those at the garnet core (175–266 ppm). The drastic increase was interpreted to be related to the progressive mixture of mafic and sedimentary components during prograde metamorphism of the sequence (Valera et al., 2021).

Some metamafic blocks exhibit similar high-Nb rutile (e.g. B214-13; Nb = 336–5,327 ppm) as well. These metamafic blocks also record enrichments in whole rock, light rare earth elements (LREEs) and Th as discussed below. In the field, these blocks are found either to contain relict metasedimentary domain (B214-7E), is adjacent to the matrix (B214-13), or is at the outermost edge of a metamafic block (B213-9 Grt+Camp+Ky; Fig. 2c). In the case of the Grt amphibolite B213-9 (Fig. 2e), the core portion of the block is kyanite-free (B213-8; Fig. 2d) and the whole rock chemistry is comparable to other Grt amphibolite blocks, i.e. flat REE pattern and no enrichment in Th relative to Ba (see below). A matrix domain

surrounding this Grt amphibolite block as a shell is currently not exposed in the field due to erosion. Matrix (B213-7; Grt+Ky) material is however observed surrounding another metamafic block nearby and was sampled in this study.

5.2 Petrography and mineral chemistry: Matrix and metasedimentary blocks

In the localities of Botoon and Nanad, two generations of matrix are identified based on their cross-cutting relationships (Valera et al., 2021). The earlier-formed matrix2a is cross-cut by matrix2b in Botoon while the former is completely transformed into blocks and are surrounded by the latter in Nanad (Fig. 2k). Both matrix2a and 2b consist of the same mineral assemblage (Botoon: Oam+Camp+Ky+Ilm; Nanad: Grt+Bt+Ilm+Ky+Camp; Fig. 3) (Valera et al., 2021). The matrix samples exhibit variable phase assemblage but always include kyanite and ilmenite (Fig. 3; Table 1). The phase assemblage of matrix samples such as B214-25 (Fig. 4a–c) and B214-2G (Fig. 4d,e) for example is similar to the Grt amphibolite blocks (Camp+Grt+Ep) except for the presence of aluminosilicates such as kyanite (and staurolite in the case of B214-2G) in these matrix samples. Others either completely lack Ca-amphibole (e.g. B213-7; Fig. 4f,g and B214-16) or have them as an accessory phase (B214-10).

The amount of garnet in the matrix samples is also variable. Some samples such as B214-1 and B214-29 (Fig. 4h,i) completely lack garnet whereas in other samples, garnet occurs abundantly either as fine euhedral grains (B213-7; Fig. 4f,g) and/or coarse porphyroclasts (N215-3; Fig. 4j-k). Replacement by Stage 3 minerals occurs in variable degree depending on the samples. The aluminosilicates in B214-2G (kyanite and staurolite; Fig. 4d,e) and B214-10 (kyanite; Fig. 4l,m) for example, are almost free of muscovite alteration (Ms3). In sample D113-21, on the other hand, Stage 2 kyanite (Ky2a) are completely lost and only fine grains of pseudomorphic muscovite (Ms3) remain (Fig. 4n,o).

The garnet grains in the matrix (matrix2a and 2b) either do not exhibit zonation or preserve a subtle zonation (e.g. Fig. 4a,b) in contrast to the garnet porphyroblasts of the blocks (Valera et al., 2021). They also have higher Mg# and lower grossular component (e.g. B214-2G Mg# = 0.44–0.47; $Grs_{16–19}$) than those in the blocks (e.g. D113-18 Mg# = 0.30–0.38; $Grs_{18–23}$; Valera et al., 2021). Ca-amphibole in the

303 matrix are also hornblende ranging from tschermakite to magnesiohornblende. Their Mg# (= 0.72–0.78)
304 are higher than the blocks and more uniform across all samples (Valera et al., 2021).

305 Rutile grains are less common in the matrix samples compared to the blocks. In samples where they
306 occur, the rutile grains preserve variable Cr-Nb concentration. Samples either have rutile with low Cr,
307 high Nb (e.g. 213-7, Cr = 89–698 ppm; Nb = 5, 215–29,695 ppm) contents or high Cr and Nb
308 concentrations (e.g. B214-2G, Cr = 376–2,319 ppm; Nb = 35–4,607 ppm) (Fig. 4p). The Cr-Nb contents
309 of rutile in the matrix do not vary with their Zr content although rutile in some samples such as B213-7 (=
310 450 ppm) have lower mean maximum Zr content (cf. Penniston-Dorland et al., 2018) than other samples
311 such as B214-2G (= 645 ppm).

312 **6 Results**

313 6.1 Whole rock geochemistry: Blocks

314 The metamafic blocks which vary from amphibolite, Grt amphibolite and to Ep amphibolites show
315 basaltic andesite (D113-15; SiO_2 = 54 wt.%) to basaltic (other samples; SiO_2 <49 wt.%) composition. The
316 mafic crust of the CPO has similar SiO_2 content. As mentioned above, earlier works on the petrogenesis
317 of the metamafic blocks suggest its genetic relationship with the mafic crust of the CPO (e.g. Keenan et
318 al., 2016). In order to constrain the effects of magmatic differentiation possibly inherited by the metamafic
319 blocks from their basaltic protoliths, binary plots with FeO*/MgO (FeO* = total Fe as FeO) as the
320 fractionation index (i.e. Fenner diagrams) are constructed (Fig. 5). The metamafic blocks along with the
321 mafic crust of the central Palawan Ophiolite exhibit decreasing CaO (Fig. 5a), MgO (Fig. 5b), Ni (Fig.
322 5c), and Cr (Fig. 5d) contents and increasing Al_2O_3, TiO_2 (Fig. 5e), FeO* (Fig. 5f), Y (Fig. 5g), and Zr
323 (Fig. 5h) concentrations with increasing FeO*/MgO.

324 There is no systematic difference between the metamafic blocks, although the amphibolites generally
325 have higher MgO, Cr, Ni and lower FeO* and TiO_2 contents at a given FeO*/MgO ratio compared to
326 garnet- and epidote-bearing varieties (Fig. 5). In the Zr-Ti-Y tectonic discrimination diagram (Pearce and
327 Cann, 1971), most of the amphibolites from earlier works plot in the MORB field together with the mafic

328 crust of the CPO (Fig. 5i). Metamafic blocks sampled in this study, on the other hand, exhibit a more
329 variable signature. A distinct group of the amphibolites, labelled gabbroic protolith in Fig. 5, have low Zr
330 contents and plot outside all tectonic fields. These metamafic blocks with low Zr contents (e.g. D113-8
331 and D113-15) have higher Al_2O_3 and CaO and lower Ni and Y concentrations compared to other blocks.
332 In the rare earth element (REE) diagrams, most metamafic blocks have flat patterns and similar
333 concentrations as the mafic crust of the central Palawan Ophiolite (Fig. 6a–c). There is also no systematic
334 difference in the REE patterns among the different amphibolite types, i.e. Ep amphibolite and Grt
335 amphibolite, although one amphibolite block (D113-11) exhibits a slight depletion in middle (MREE) to
336 heavy rare earth elements (HREE; Fig. 6b). The low-Zr metamafic blocks (e.g. D113-8 and D113-15) also
337 have the lowest REE concentrations (Fig. 6a–c). Their LREEs are also slightly depleted such as in the
338 amphibolite block B213-04 (La_N/Sm_N = 0.48) and a distinct positive Eu anomaly (Eu/Eu*=3.08) is notable.
339 One sample of each amphibolite type, i.e. the Ep amphibolite (B214-7E), amphibolite (B214-13), and Grt
340 amphibolite (B213-9) blocks are also enriched in LREEs. These blocks either contain a relict
341 metasedimentary domain or are found adjacent to the surrounding matrix (see section 5.1).
342 The metamafic blocks and the mafic crust of the CPO also generally show similar trends in an
343 extended trace element spidergram (Fig. 6d–f). This include enrichments in fluid mobile elements such as
344 Rb, Ba, U, Pb and Sr. Some notable difference between the metamafic blocks and the mafic crust of the
345 CPO is the enrichment in Nb and Ta in the former (Fig. 6). The low-Zr metamafic blocks also have lower
346 trace element concentrations than the other metamafic blocks. They also exhibit positive Sr anomaly not
347 seen in the other amphibolite and Grt amphibolite blocks. The low-Zr Grt amphibolite blocks (i.e. D113-
348 14G, D113-15) also show positive Ti anomalies. The LREE-enriched metamafic blocks exhibit marked
349 enrichment in Th, Nb, Ta. In contrast, negative Ti anomalies were observed in the Ep amphibolite and
350 amphibolite blocks.
351 6.2 Whole rock geochemistry: Matrix and metasedimentary blocks

Samples which consist of matrix2a alone and those including both matrix2a and 2b do not exhibit systematic difference in whole rock major and trace elements compositions (Fig. 7a–f). The matrix surrounding the blocks exhibits variable phase assemblages as well as distinct geochemical characteristics compared with the metamafic blocks. The Al_2O_3 (Fig. 7a) and Zr contents of the matrix increase with their TiO_2 concentration and are generally higher compared to the metamafic and metasedimentary blocks (Fig. 7a). Direct correlation is also found between their Cr content and whole rock Mg# (Fig. 7b) and La vs Th (Fig. 7c) concentrations of the matrix samples. Distinct signatures are observed for more fluid-mobile elements in the matrix samples. Their CaO (Fig. 7d) and SiO_2 (Fig. 7e) concentrations are generally lower at a given FeO*/MgO ratio compared to the metamafic blocks while K_2O, Ba and Rb contents of the matrix are higher (Fig. 7f). The latter group of elements also exhibit positive correlation with each other (Fig. 7f). The concentrations of these three elements (K_2O, Ba and Rb) in the matrix samples are linked to the degree of Stage 3 replacement in the matrix. For example, the matrix 2a D113-21 with kyanite grains completely replaced by fine pseudomorphic muscovite (Ms3; Fig. 4n,o) have higher K_2O, Ba and Rb contents than B214-2G (Fig. 4d,e) which largely preserves its aluminosilicates (e.g. kyanite and staurolite).

Except for the metacarbonate block B214-7C, the metasedimentary blocks generally exhibit the same trends in terms of major oxide concentrations as the matrix surrounding them. The Cr (= 28–1045 ppm) and Ni (= 71–632 ppm) contents of the matrix samples are comparable with the metamafic blocks (Cr = 14–966 ppm; Ni = 20–680 ppm) at a given FeO*/MgO (Fig. 7b). These values are higher than the metasedimentary blocks (Cr = 49–459 ppm; Ni = 51–174 ppm) but are much lower than the overlying ultramafic rocks of the Palawan Ophiolite (Cr = 1528–3072 ppm; Ni = 1045–2499 ppm).

The REE contents of the metasedimentary block and matrix samples normalized to NMORB (Hofmann, 1988) are shown in Fig. 8a and b. In contrast to most metamafic blocks, all matrix samples exhibit elevated LREEs ($(La_N/Sm)_N$ = 4.90–8.33). All samples also show a negative Eu anomaly (Eu/Eu* = 0.55–0.96; Eu* = $(Sm*Gd)^{1/2}$). Similar to the metamafic blocks however, the M-HREEs of the matrix samples are flat. The metasedimentary blocks, aside from B214-26, shows the same elevated LREEs and

flat M-HREEs as the matrix (Fig. 8a). The Ky-Ilm-Grt quartzite (N215-4) block shows the same slightly negative Eu anomaly (Fig. 8a). The metasedimentary block sample B214-26 exhibits a flat REE trend with concentrations comparable to NMORB.

In contrast to the metamafic blocks, the matrix samples (Fig. 8c–d) and the metasedimentary block N215-4 (Fig. 8a–b) both record negative Ba, Nb, Sr, and Ti anomalies in an extended trace element spidergram. The metacarbonate block B214-7C exhibits distinct trends relative to other metasedimentary blocks such as a depletion in Rb, and enrichments in Th, U, and Pb (Fig. 8c). In the extended trace element spidergram, both matrix2a only and matrix2a-2b samples show the same trend characterized by elevated incompatible elements i.e. Rb, Ba, Th, U (Fig. 8d) and depletion in Nb and Ta.

6.3 Correlation coefficient (*r*)

In order to distinguish the effects of mechanical mixing, fluid advection and other controls on the petrological characteristics of the matrix samples, the procedural work flow illustrated in Fig. 9 was used. First, Pearson product-moment coefficient of correlation (*r*) was applied (Sachs, 1984). This calculation measures the strength of linear association among the suite of major and trace elements and helps identify which elements behave similarly, i.e. exhibit strong positive correlation with one another. The correlation coefficients shown as matrices in Table 4 are based on the expression:

Eqn. 1 $$r = \frac{n\sum(xy) - \sum(x)\cdot\sum(y)}{\sqrt{[n((\sum x^2) - (\sum x)^2)]\cdot[n((\sum y^2) - (\sum y)^2)]}}$$

where n (= 12) represents the number of matrix samples and x, y variables are the concentration of the elements being correlated. A 5% significance level limit of r = 0.497 for a degree of freedom (DF) of 10 (DF = $n-2$) was used (Sachs, 1984).

If advection is the dominant process, elements mobilized by the fluids should either exhibit systematic enrichment or depletion in the affected rocks, depending on the stability of sink minerals of such elements. Fluid-immobile elements however, will not be affected and will remain in the rock. Their concentration in the rock will thus change systematically depending on whether fluid-mobile elements are

added or removed from the rock volume (Gresens, 1967; Grant, 1986). Meanwhile, if mechanical mixing is prevalent then at least two groups of elements should emerge, each representing an end-member component. It is however possible that both processes coupled by other factors, e.g. phase assemblage control, could have affected the matrix samples. In order to address this possibility, the correlation coefficient among fluid-immobile elements is investigated.

Based on the calculated correlation coefficients (Fig. 10a, Table 4), at least two groups of fluid-immobile elements are identified. Group 1 elements include TiO_2, Al_2O_3, Zr, Th and LREEs (diamond symbols in Fig. 10a). The concentration of Th, Zr and the LREEs in the matrix samples in particular show very high correlation coefficients, e.g. the correlation coefficient between Th and La (Th-La) is $r = 0.99$. These group of elements exhibit strong negative correlation with the whole rock Mg#, SiO_2 and Na_2O contents of the matrix samples (Fig. 10a). Group 2 (cross symbols in Fig. 10a) includes Cr, Ni (Cr-Ni correlation coefficient $r = 0.88$) and MgO which are all negatively correlated with the TiO_2 (e.g. Cr-TiO_2 $r = -0.72$) and FeO* (e.g. Cr-FeO* $r = -0.65$) contents of the matrix samples (Fig. 10a).

The distinct grouping of these elements suggest end-member components contributing to the chemistry of the matrix samples. In particular, the context of a slab-mantle wedge interface for the Dalrymple Amphibolite (Valera et al., 2021) suggests the possibility of mechanical mixing among crustal (sedimentary and mafic) lithologies from the subducting slab and/or an ultramafic end-member from the hanging wall. This information will be used in identifying the end-members and mixing ratio estimation discussed below. Two more groups of elements which also exhibit positive linear correlation with one another are identified. Group 3 includes MnO (circles in Fig. 10a) which is strongly correlated with the Nb, Ta and the HREEs of the matrix. Group 4 is the large ion lithophile elements: K_2O, Ba and Rb (triangles in Fig. 10a).

6.4 Mixing ratio estimation

Regression analysis was performed to identify the most likely end-members controlling the concentration of Groups 1 and 2 elements/components in the matrix samples and the mixing proportion of these end-members. This was done by fitting the concentration of Cr, Ni, Zr, TiO_2, and Al_2O_3 (assumed to be immobile) of the measured and modelled matrix compositions using least squares method (Figs. 4; 10b). The modelled matrix composition was obtained by changing the end-members used and their relative proportions. The combination of end-members and corresponding mixing proportion with the highest coefficient of determination for linear regression (r^2) was then utilized to calculate the concentration of other elements in the modelled matrix.

A caveat must be given on the assumption that Al_2O_3 is immobile. Valera et al. (2021) reported quartz-kyanite veins transecting the Dalrymple Amphibolite which could indicate either the mobility of Al_2O_3 similar to what was documented for the Alpe Sponda Orogenic Belt (Beitter et al., 2008) or the extreme leaching of the other components that left behind relatively immobile components (Al_2O_3 and TiO_2). The latter is favored by the Valera et al. (2021) based on the abundance of ilmenite-kyanite accumulations in the matrix2a and 2b samples (Table 1). The mobility of the Al_2O_3 cannot be ruled out altogether however especially considering the relatively high peak *T* conditions.

In this work, two lines of evidence support the utilization of Al_2O_3 in the mixing ratio estimation. First, the high correlation coefficient between Al_2O_3 and other Group 1 elements and its negative correlation with Group 2 elements (Fig. 10a) strongly suggest that the concentration of this element in the matrix is controlled by the mixing proportion between end-members. This also suggests that the bulk concentration of Al_2O_3 in the matrix was not significantly affected by selective mobilization due to infiltrating fluids and/or partial melting. Second, minimizing the effect of Al in the regression analysis by changing the denominator, for example Al/500 or Al/1000 (supplementary file Fig. S1) instead of Al/100 in Fig. 10b, does not significantly affect the relative ranking of matrix samples with regard to which samples have higher or lower metased1:metamafic2 ratios. This is best illustrated when ranking the metased:metamafic ratios of modelled matrix samples using metased1 and metamafic2A end-members

449 (Fig. S1 vs. Fig. 10b) as discussed in section 7.2. These constraints indicate that although the possible
450 mobility of Al_2O_3 could not be completely ruled out in this study, it does not significantly affect the
451 subsequent interpretations and conclusions.

452 The high values of Group 1 elements in the matrix samples, especially Zr, Th and the LREEs,
453 suggest a metasedimentary end-member. A possible end-member, the Ky+Ilm+Grt quartzite block N215-
454 4, was selected from the metasedimentary blocks, referred hereafter as simply metased1. This is supported
455 by the remarkable similarity in REE and trace element pattern among matrix samples which is the same
456 as the trends in the block sample N215-4 (Fig. 8a,c). Other possible sedimentary end-member values such
457 as the North American shale composite (NASC; Gromet et al., 1984), average South China Sea sediment
458 (Li et al., 2003) were considered for metased1 but consistently resulted to lower r^2 values.

459 Group 2 elements/components (Cr, Ni and MgO) can indicate either a mafic or an ultramafic end-
460 member. An ultramafic end-member is not considered since such an end-member is inconsistent with the
461 following lines of evidence: 1. Neither blocks of ultramafic composition nor highly Mg-rich matrix, i.e.
462 dominated by serpentine+talc+Mg-chlorite, was observed in the Dalrymple Amphibolite; 2. The dunite-
463 harzburgite interlayers overlying the Dalrymple Amphibolite are relatively fresh with the serpentine
464 phases replacing some olivine and pyroxenes in the ultramafic rocks being predominantly low-*T* species
465 (e.g. chrysotile and lizardite); 3. The *P-T-D* conditions of the Dalrymple Amphibolite are above the
466 stability field of serpentine (Valera et al., 2021). Numerical modelling (Gerya et al., 2002; Agard et al.
467 2016) revealed that deformation and incorporation of basalts rather than "fresh" unserpentinized mantle
468 material as matrix material is most likely at these *P-T* conditions due to the rheological strength of the
469 latter relative to the former.

470 The end-member likely controlling Group 2 elements/components was therefore selected from the
471 metamafic blocks of this study, the average central Palawan Ophiolite basalt (data from Encarnacion et
472 al., 1995 and Keenan et al., 2016), and the average normal MORB (NMORB; Hofmann, 1988). The
473 highest r^2 values are obtained when the amphibolite block D113-9 (metamafic2A) is used as end-member

474 for some samples (Table 5) and the Ep amphibolite D113-5 (metamafic2EA; Table 5) for others (Fig. 10b).
475 We selected the metamafic end-member with the highest regression value depending on the matrix
476 samples (Table 5).

477 In order to account for the difference in the concentration between the major oxides and trace
478 elements, which affects the regression value vis-à-vis the proportion between end-members, the ratios
479 Ti/10 and Al/100 were utilized. The metased1: metamafic2(A or EA) ratio with the highest coefficient of
480 determination for linear regression (r^2) is then used to obtain the complete set of modelled composition of
481 the matrix sample given in Table 5. These modelled values are interpreted to correspond to the original
482 composition of the matrix samples which was subsequently affected by infiltrating fluids (as discussed in
483 more detail in the Discussion section). These modelled values were thus used as the 'original' composition
484 in the mass balance calculation (isocon analysis).

485 The coefficients of determination for linear regression (r^2) are high ranging from 0.88–0.99 (Fig.
486 10b). The metased1 / (metased1 + metamafic2A/EA) ratios are high, generally above 50% except for
487 N215-3 (31%) and B214-29 (49%; Fig. 10b). One matrix sample B214-25, shows the highest r^2 value
488 when the metased1: metamafic2EA ratio is at a minimum, i.e. zero (Fig. 10b). The trace element content
489 of this matrix sample, however, exhibit enrichments in LILE (e.g. Th) and LREEs similar to the other
490 matrix samples (Fig. 8c,d). The sample is mainly composed of Ca-amphibole with minimal (<5%) garnet
491 and kyanite partly replaced by muscovite (Fig. 4a–c). Compositional maps of the garnet porphyroblasts in
492 this sample (Fig. 4b) revealed the same chemical zonation pattern characteristic of garnets in the matrix,
493 i.e. higher Mg# and subtle change in chemistry from core to mantle, in contrast to the garnet porphyroblasts
494 of the blocks (Valera et al., 2021). These contrasting signatures present the limitation of the method applied
495 in this study in estimating the mixing ratio. This sample is not considered further in the isocon analysis
496 since its 'original' composition cannot be determined.

497 Small differences in the concentration of some major elements/components, e.g. TiO_2 and CaO,
498 between the two metamafic end-members used inevitably resulted to modelled matrix compositions with
499 slightly different trends (e.g. Fig. 7e). Comparing the modelled against the measured matrix composition
500 as a whole however reveals similar characteristics regardless of whether the amphibolite block D113-9
501 (metamafic2A) or the Ep amphibolite block D113-5 (metamafic2EA) is used. The modelled matrix
502 compositions show lower TiO_2, Al_2O_3 (Fig. 7a), Zr, La, Th (Fig. 7c) than the measured matrix
503 concentration. The concentration of these elements/components in the modelled matrix are more similar
504 to the metamafic and metasedimentary blocks. The CaO (Fig. 7d) and SiO_2 (Fig. 7e) contents of the
505 modelled matrix meanwhile are intermediate between the metamafic and metasedimentary end-member
506 blocks and higher than the measured matrix. The opposite is true for the concentrations of K_2O, Rb, and
507 BaO in the modelled matrix which are consistently higher in the measured matrix (Fig. 7f). The REE (Fig.
508 8e) and extended trace element pattern (Fig. 8f) of the modelled matrix also largely reproduced the trends
509 and concentrations observed in the matrix samples. Such signatures include enrichment in LREEs and Th,
510 and negative anomalies in Eu, Ba, Nb, Sr, and Ti. Differences exist with regard to La and Ta which are
511 slightly enriched relative to Ce and Nb, respectively, in the calculated matrix (Fig. 8e,f). Such trends are
512 not observed in the measured matrix data (Fig. 8b,d). The use of two different metamafic end-members
513 did not also affect the trace element concentrations and trends of the modelled matrix.

514 6.5 Mass balance calculations: Isocon analysis

515 The interaction between infiltrating fluids and surrounding wall rock in metasomatic environments
516 such as the slab-mantle wedge interface can result in the removal and/or addition of elements to the
517 surrounding rocks (e.g. Bebout, 2013). The mass change during these metasomatic events can be
518 calculated from the initial and final concentrations of element *i* and the ratio of the final to initial volume
519 of the rock in question (Gresens, 1967; Grant, 1986). Alternatively, the mass change (m_0/m_a) can be
520 calculated graphically by plotting the concentration of each component *i* in the affected (i.e.
521 metasomatized) and in the original rock (unmetasomatized). Connecting the concentration of elements

assumed to have not moved during metasomatism (i.e. immobile elements) through the origin defines the isocon line. The relative gain or loss of the other elements can then be calculated using Eqn. 2 (Gresens, 1967; Grant, 1986):

Eqn. 2 $$\frac{\Delta C_a^i}{C_0^i} = \left(\frac{m_a}{m_o}\right) \cdot \left(\frac{C_a^i}{C_0^i}\right) - 1$$

where C_a^i and C_0^i is the final and initial concentrations of element i respectively. The ΔC_a^i is the change in the concentration of element *i* relative to its concentration prior to alteration and $(m_a/m_o)^{-1}$ is the slope of the isocon line. The Microsoft excel-based EASYGRESGRANT (Lopez-Moro, 2012) was used in the mass balance calculations for the matrix samples assuming TiO_2, Al_2O_3, Cr, Nd, Zr, and Hf as immobile. The modelled composition of the matrix samples is used as the original (unmetasomatized) rock while the measured composition of the samples is considered to be the affected (metasomatized) rock.

The relative gains and losses in the matrix samples calculated graphically from the isocon line is best represented as the ratio of the change in concentration of element *i* to the original concentration of the element ($\Delta C_a^i / C_0^i$), calculated using Eqn. 2 (Fig. 11a–e; Lopez-Moro, 2012). The isocon line was defined by fitting TiO_2, Al_2O_3, Cr, Nd, Zr and Hf with a line passing through the origin using the least squared method. Aside from these assumed immobile elements/components, FeO* and the LREEs (except Ce) exhibit general immobility, i.e. showing neither relative gain or loss.

The matrix samples exhibit consistent loss in SiO_2, CaO, and P_2O_5 (Fig. 11a). Some matrix samples record gains in MnO, Na_2O, Ba, Nb, Ta, and in M-HREEs while others show relative losses in these elements/components. These relative gains or losses appear to be closely linked to the phase assemblage of the matrix. The garnet-rich matrix2a sample B213-7 (Fig. 4f,g), for example, shows relative gains in MnO, Nb, Ta and HREEs. Another garnet-bearing matrix 2a-2b sample N215-3 (Fig. 4 j,k) shows minimal losses in these elements (Fig. 11d). Matrix samples like B214-1, B214-16 and B214-29 (Fig. 4h,i), which completely lack garnet, show significant losses in these elements (Fig. 11d). An exemption to this is B214-

2G (Fig. 4d,e) which contain coarse garnet porphyroblasts but also exhibits loss in Mn and HREEs (Fig. 11d). Rutile grains equilibrated with zircon and quartz in this sample however show higher Zr-concentration (= 645 ppm) than rutile found in B213-7 (= 450 ppm) or N215-3 (= 318 ppm). Losses expressed as $\Delta C_a^i/C_0^i$ in terms of MgO, Cr (Fig. 11b), CaO, and Na_2O (Fig. 11c) are also minimized in hornblende-rich samples such as B214-2G (MgO = +0.63; Cr = +0.33; CaO = −0.24; Na_2O = −0.43; Fig. 4d,e) and B217-2 (MgO = +0.26; Cr = +0.11; CaO = −0.28; Na_2O = −0.03), compared to the hornblende-poor matrix sample B214-10 (MgO = −0.16; Cr = −0.11; CaO = −0.92; Na_2O = −0.93; Fig. 4l,m) which is largely composed of kyanite and biotite.

All matrix samples exhibit gains in Th and Ce. A few of the matrix samples exhibit loss in K_2O and Rb while the majority record variable gains in these elements. Matrix samples which either incurred a loss in K_2O and Rb (B214-2G) or did not show any change in concentration of these elements (B214-10), preserve their Stage 2 minerals, especially kyanite (Ky2), compared to the moderate to extensive degree of Stage 3 replacement observed in other matrix samples.

As mentioned above, some of the metamafic blocks exhibit enrichment in LREEs and incompatible elements (e.g. Th) similar to the matrix surrounding them. In the case of B213-9, the whole rock composition of the core of the block (B213-8) do not show such enriched signatures and preserves a flat REE pattern (Fig. 6c,f). In order to determine if the same process which formed the matrix affected this block, we utilized the same procedure of mixing ratio estimation and isocon analysis applied to the matrix samples.

In estimating mixing proportion, the whole rock composition of the surrounding matrix (B213-7) and the core of the Grt amphibolite block (B213-8) were used as end-members. Cr, Ni, Zr, TiO_2 and Al_2O_3 contents of B213-9 were fitted with variable proportions of metamafic (B213-8) and matrix2a (B213-7). The resulting matrix / (matrix + amphibolite) ratio was low (11%, r^2 = 0.99). Mass-balance calculation was done using the kyanite-bearing Grt amphibolite B213-9 as the metasomatized rock volume and the

kyanite-free Grt amphibolite block B213-8 as the original (unmetasomatized) composition. The fluid immobile elements/components TiO_2, Al_2O_3, Cr, Nd, Zr, and Hf were also used to fit an isocon through the origin. The results revealed neither gain nor loss in most elements ($\Delta C_a^i/C_0^i = \pm 0.2$) while more mobile elements such as K_2O ($\Delta C_a^i/C_0^i = -0.6$), Rb ($\Delta C_a^i/C_0^i = -0.6$), and P_2O_5 ($\Delta C_a^i/C_0^i = -0.7$) record losses.

7 Discussion

7.1 Origin of the metamafic blocks

The increasing FeO* and TiO_2 (Fig. 5e,f) with magmatic differentiation, i.e. increasing FeO*/MgO, observed in the mafic crust of the CPO are consistent with a tholeiitic magmatic series typical of MOR lavas (e.g. Irvine and Baragar, 1971). A MOR tectonic setting of formation is further supported by the Zr-Ti-Y plot where the CPO lithologies fall in the MORB field (Fig. 5i), as well as their flat trends in the NMORB-normalized REE diagrams (Fig. 6a-c). In contrast to NMORB, the mafic crust of CPO exhibit enrichment in LILEs such as Rb, Ba, U, Pb and Sr (Fig. 6d-f). Earlier works suggest that such enriched signature indicate that these lavas are tholeiites formed in a transitional island arc (IAT) tectonic setting (Keenan et al., 2016; Gibaga et al., 2020). Depletion in HFSEs such as Nb, Ta, Zr characteristic of IAT lavas (Tatsumi, 2005) are however not observed in the mafic crust of the CPO. Alternatively, the LILE enrichment is more likely related to in-situ hydrothermal alteration of the mafic crust of the ophiolite which is prevalent in mid-oceanic ridge spreading centers (e.g. Bebout, 2013; Starr and Pattison, 2019). This interpretation is also more consistent with its genetic relationship with the metamafic blocks of the Dalrymple Amphibolite discussed below.

The magmatic differentiation trends exhibited by the mafic crust of CPO are largely preserved in the metamafic blocks (Figs. 5,6). This is evidenced by the decreasing trend of compatible elements/components such as CaO (Fig. 5a), MgO (Fig. 5b), Ni (Fig. 5c), Cr (Fig. 5d) and increase in incompatible elements such as Y (Fig. 5g) and Zr (Fig. 5h) with increasing FeO*/MgO values. The tholeiitic basalt signature of the mafic crust of CPO, i.e. increasing TiO_2 (Fig. 5e) and FeO* (Fig. 5f) and flat REE trends (Fig. 6a–c), are also preserved by most metamafic blocks. Similar enrichments in LILEs

such as Rb, Ba, U, Pb, and Sr are also observed in both the mafic crust of CPO and the metamafic blocks (Fig. 6d–f). These lines of evidence suggest the genetic relationship of the Dalrymple Amphibolite with the mafic crust of CPO. In particular, basaltic lavas similar to the CPO likely served as the protolith for the metamafic blocks. This supports the existing model of a spreading center-turned subduction zone model for the Palawan Ophiolite (Keenan et al., 2016; Dycoco et al., 2021; Valera et al., 2021). According to this model, the Dalrymple Amphibolite represents the subducted oceanic lithosphere whereas the other half of the oceanic lithosphere is now emplaced as the CPO.

The low-Zr metamafic blocks with low concentrations of incompatible elements such as Y (Fig. 5g) and Zr (Fig. 5h) and higher amounts of Al_2O_3 and CaO (Fig. 5a) at a given FeO*/MgO ratio suggest a distinct protolith. These geochemical signatures as well as the positive Eu and Sr anomalies in the extended trace element plot (Fig. 6), and slight depletion in LREEs are comparable to MOR-cumulate gabbros (e.g. Kelemen et al., 1997). These blocks therefore likely represent the metamorphosed equivalent of deeper sections of the subducting oceanic lithosphere, i.e. cumulate gabbro section. Such interpretation is consistent with higher An-content of plagioclases in these block samples compared to other metamafic blocks (Valera et al., 2021) indicating an overall higher CaO/Na_2O budget of their mafic protolith. Lastly, the LREE-enriched blocks exhibit similar REE and extended trace element trends as the metasedimentary blocks and the matrix surrounding the blocks (Fig. 6d–f). Their petrogenesis are discussed further in the subsequent section.

7.2 Mixing of sedimentary-mafic components: Initial clues and limitations of the modelled matrix composition

The *P-T-D* history of the Dalrymple Amphibolite revealed the timing of deformation events which led to its block-in-matrix configuration (Valera et al., 2021). It was shown that matrix-forming processes started as the whole sequence was being subducted towards peak metamorphic conditions (~700 °C, 13 kbar). The variation in Nb content of rutile grains in the block sample B214-21 (Fig. 4p; Valera et al., 2021) provides evidence of the relative timing of mixing between sedimentary and mafic end-members.

619 Rutile included in the garnet cores (Stage 1a) have low Nb concentrations and indicate a metamafic
620 protolith while those in the garnet rim and matrix (Stage 1b) record a ten-fold increase in Nb content and
621 plot into the metapelite field (Fig. 4p; Valera et al., 2021). The similar peak metamorphic conditions
622 preserved in the matrix compared with the blocks and the successful pseudosection modelling of the
623 matrix2a sample B214-10 by Valera et al. (2021) further indicate that such mixing process in the matrix
624 was largely completed before the sequence reached peak *P-T* condition. The Nb and Cr contents of rutile
625 grains in some blocks especially in B214-13 (Fig. 4p) also hint mixing between metamafic and
626 metasedimentary end-member components.

627 A more comprehensive view on the mixing process that operated in this shear zone can be
628 established by looking at the whole rock composition of the sheared matrix surrounding the blocks. The
629 distinct grouping of elements, identified based on their correlation coefficient (Fig. 10a), suggests the
630 strong control of two end-member components in the chemistry of the matrix samples. The
631 metasedimentary end-member controlled the Al_2O_3, TiO_2, Zr and LREEs composition (Group 1
632 elements/components) of the matrix whereas the metamafic end-members (metamafic2A and 2EA) are
633 linked with Group 2 elements/components such as MgO, Cr and Ni. Such distinct grouping of fluid-
634 immobile elements/components with similar behavior suggests that mechanical mixing of these two end-
635 member components was indeed the predominant process in this slab-mantle wedge interface locality.

636 In other high-*P/T* type metamorphic terranes, mixing ratios are estimated using stable isotopes of
637 highly siderophile elements (e.g. $^{187}Os/^{188}Os$; Gorman et al., 2019). The limited involvement of ultramafic
638 end-member in the mixing process in the Dalrymple Amphibolite however made application of this
639 technique inappropriate. As discussed in sections 6.3 to 6.4, this study identified end-members and
640 estimated their mixing ratios using fluid-immobile elements which are representative of each end-member
641 (metased1: Al_2O_3, TiO_2, and Zr; metamafic2A and 2EA: Cr and Ni). The regression analysis using only
642 major and trace elements done in this study, however, has its own limitations. In order to account for the

643 difference in the concentration between the major oxides and trace elements, the ratios Ti/10 and Al/100
644 were utilized. These values were selected because they represent a satisfactory spread of elements along
645 the linear regression line for most samples (Fig. 10b). Changing the denominator values e.g. Al/1000,
646 Ti/100 and Ti/50, Al/500, also changes the value for the best-fit ratio between the end-members albeit
647 mostly within a margin of ±12% except D113-21 (±26%) and B214-16 (±31%). Despite changes in the
648 metased1/(metased1 + metamafic2A/EA) ratios, the relative ranking of the matrix samples with regard to
649 which samples have higher or lower metased1:metamafic2A/EA ratios, is more uniform (Fig. S1 vs. Fig.
650 10b). The results of mass balance calculations which depend on the modelled matrix composition as the
651 original (unmetasomatized) rock volume, do not also change in terms of elements that were lost or gained.

652 This limitation nonetheless highlights that the metased1: metamafic2A/EA ratios (Fig. 10b, Table
653 5) cannot be treated as absolute values but are better utilized as qualitative measure of mixing between the
654 metasedimentary and metamafic end-members which controlled the chemistry of the matrix of the
655 Dalrymple Amphibolite. The subsequent discussion on mixing and mass balance calculations are therefore
656 drawn considering the metased1/(metased1 + metamafic2A/EA) ratios not as absolute values but rather as
657 qualitative measures of metasedimentary-metamafic ratios. More importantly however, this procedural
658 workflow allowed this study (1) to estimate the 'original' bulk composition of the matrix (i.e. modelled
659 matrix composition), and (2) to distinguish the effect of fluid infiltration through mass balance calculations.
660 The validity of the procedure employed in this study can be assessed by looking at how consistent the
661 modelled matrix composition and mass-balance calculations are with the observed petrological
662 characteristics (Section 7.4).

663 The measured whole rock composition of the matrix records the lowest values in terms of fluid
664 mobile elements such as CaO, SiO_2 and Na_2O (Fig. 7d,e). The metasedimentary blocks also register
665 comparably low concentrations of these elements. The measured matrix composition also records
666 pronounced enrichment in some fluid immobile elements/components, most notably Zr and Al_2O_3 (Fig.

667 7a) and less mobile elements La and Th (Fig. 7a–c). One possible explanation for such signatures is the
668 preferential leaching of fluid mobile components (e.g. CaO, SiO_2, Na_2O) which left behind more immobile
669 elements/components (e.g. Zr, Al_2O_3). As will be discussed in more detail in the subsequent section, the
670 preferential retention of immobile components such as Al_2O_3 and TiO_2 during leaching is consistent with
671 the abundance of kyanite and ilmenite in the matrix (Table 1).

672 In order to assess the characteristics of the original whole rock composition of the matrix (i.e. pre-
673 leaching), the modelled matrix composition can be utilized. Notably, the whole rock CaO, Na_2O (Fig. 7d),
674 and SiO_2 (Fig. 7e) contents of the modelled matrix is intermediate between the metamafic and
675 metasedimentary blocks. A more CaO- and Na_2O-rich whole rock composition could explain the
676 abundance of Ca-amphibole in the matrix samples and may reflect its metamafic roots. This is further
677 supported by the mass balance calculations wherein losses in MgO and Cr (Fig. 11b), as well as CaO and
678 Na_2O (Fig. 11c) are generally minimized in the hornblende-rich matrix samples (e.g. B214-2G; Fig. 4d,e)
679 compared to the hornblende-poor samples (e.g. B214-10; Figs. 4l–m, 11b–c). The similarity in LREE and
680 trace element patterns and concentrations of the modelled (Fig. 8e,f) and measured matrix compositions
681 (Fig. 8b,d) supports the inference of a metasedimentary end-member in the mixing process. The
682 remarkable similarity in the trace element patterns of the measured and modelled matrix samples and the
683 metasedimentary block N215-4 also indicate the strong control of this end-member on the trace element
684 content of the matrix. The interpretations drawn from the whole rock composition of the matrix samples
685 are also consistent with their petrographic characteristics and trace element content of rutile in the matrix.

686 Exhibiting highly variable mineralogy, most matrix samples consist of minerals more commonly
687 observed in metapelites (e.g. kyanite-biotite in B214-10; Fig. 4l,m) as well as assemblages dominated by
688 Ca-amphibole and/or garnet reminiscent of the metamafic blocks (N215-3; Fig. 4j,k). This is exemplified
689 by the matrix2a sample B214-2G which contains abundant aluminosilicates (Grt+Ky+St), along with
690 biotite and hornblende (Fig. 4d,e) and of B214-29 (Ky+Camp+Oam; Fig. 4h,i). The rutile grains of the
691 matrix samples also exhibit variable Nb-Cr concentrations within each sample as well as within a single

692 grain (i.e. core vs. rim). Looking at it as a whole however, the Cr-rich rutile (e.g. N215-3 Cr = 1,115–
693 13,102 ppm), indicating metamafic protolith, and/or Nb-rich rutile (e.g. N213-7 Nb = 4,369–29,695 ppm),
694 typically found in metasedimentary blocks, are both observed in the matrix samples (Fig. 4p).

695 7.3 Fluid infiltration: Stages and imprints on the matrix samples

696 The effect of fluid-rock interaction in the relative gains and losses in certain elements throughout
697 the *P-T-D* history of the Dalrymple Amphibolite was assessed using isocon analysis (Fig. 11a–e). Mass
698 balance calculation and the petrological characteristics of the matrix samples suggest distinct stages of
699 fluid infiltration which had contrasting effects on the sheared matrix samples. The presence of ilmenite,
700 kyanite, and zircon in the matrix is consistent with the assumption in the isocon analysis which considered
701 TiO_2, Al_2O_3, Zr, and Hf as immobile, i.e. retained in the rock as leaching progressed. This is exemplified
702 by the matrix sample B214-10 (Fig. 4l,m) dominated by coarse euhedral kyanite and high concentrations
703 of ilmenite in the interstices. The matrix samples also appear to have retained their original FeO* content
704 (Fig. 11a). The preferential retention of this relatively mobile element is again most likely due to the
705 widespread stabilization of ilmenite in all matrix samples (Table 1). In contrast, other fluid-mobile
706 elements such as SiO_2, CaO and P_2O_5 record losses. The depletion in fluid-mobile components (e.g. CaO,
707 SiO_2, Na_2O) and enrichment in fluid-immobile elements/components especially Al_2O_3, Zr, La, and Th in
708 the measured matrix relative to the modelled matrix indicate the predominant leaching effect of these
709 infiltrating fluids.

710 The control of phase assemblage on the variable degree of loss of elements in the matrix during the
711 leaching process is even more apparent when we look at the relative loss of Mn, HREEs and Y in the
712 matrix samples (Fig. 10b–e). The high correlation coefficients of these elements (Fig. 10a) suggest similar
713 behavior which was likely controlled by the presence or absence of garnet in the matrix sample. This is
714 evidenced by the mass balance calculations which feature garnet-rich samples either retaining their
715 original composition (e.g. B213-7; Figs. 4f,g, 11d) or whose losses in these elements are minimal (e.g.

716 N215-3; Figs. 4j–k, 11d) relative to samples which completely lack garnet (e.g. B214-29; Figs. 4h–i, 11d).
717 Relative losses in the fluid-mobile elements Ca and Na are also apparently linked to the abundance of Ca-
718 amphibole in the matrix samples. As noted above, loss in Ca and Na are minimal in hornblende-rich
719 matrixes (e.g. B214-2G; Fig. 4d–e, 11c), compared to the hornblende-poor matrix sample such as B214-
720 10 (Figs. 4l–m, 11c).

721 The strong control of phase assemblage in the degree of leaching in matrix samples further suggest
722 that this fluid-infiltration event likely occurred early (Stage 2) in the *P-T-D* history of the Dalrymple
723 Amphibolite, i.e. as the matrix-forming minerals such as kyanite, ilmenite, garnet and hornblende were
724 being formed. The variable degree of loss in some elements (e.g. CaO, NaO, M-HREEs, Y) from the
725 matrix of the Dalrymple Amphibolite indicates that the stabilization of sink minerals (e.g. Al_2O_3 in kyanite;
726 TiO_2 and FeO* in ilmenite) is required prior to the leaching process for the retention of these elements
727 within the matrix (Figs. 12a, c, d). Such fluid-infiltration may have been promoted by the shearing and
728 mixing of metasedimentary and metamafic end-members, as the slab-mantle wedge interface lithologies
729 were being deformed into its current block-in-matrix configuration (Fig. 12 c,d). Losses during this early
730 fluid infiltration are more uniform among matrix samples, that is the values of $\Delta C_a^i / C_0^i$ are relatively small
731 ranging from 0 to -1 (Fig. 10b–f), suggesting the pervasive nature of the fluid infiltration.

732 The early timing of fluid infiltration resulting in leaching of certain elements from the original
733 matrix samples is supported by the high degree of loss in Mn, HREEs and Y recorded by B214-2G (Figs.
734 6e; 11d) compared to B213-7 (Figs. 6g, 11d). Both are garnet-rich samples and contain rutile grains
735 equilibrated with zircon and quartz. The rutile grains in B214-2G hosted in hornblende and garnet record
736 higher Zr content indicating a higher peak *T* (= ~730 °C at 13 kbar following Tomkins et al. 2007)
737 compared with B213-7 (= ~700 °C at 13 kbar; Fig. 12a). This possibly indicates that the infiltrating fluids
738 may have already leached out Mn, HREEs and Y from B214-2G before it crystallized the rutile-hosting
739 hornblende and garnet at higher *T*. Early crystallization of garnet in B213-7 enabled the retention of these

elements, which is supported by low-Zr rutile grains (i.e. low-*T* rutile grains) found in this sample (Fig. 12a). The estimated *P*-*T* conditions of fluid infiltration and leaching are close to the peak metamorphic conditions recorded in the matrix (Stage 2; Fig. 1c) and are consistent with the interpretations of Valera et al. (2021) that matrix-forming processes (i.e. mixing, fluid infiltration, and deformation) were active as the sequence was being subducted towards greater depths.

Similar to the leaching out of fluid-mobile elements/components (e.g. SiO_2 and CaO), losses in K_2O, Ba, and Rb were likely originally preserved in the matrix sample. This is still recorded in B214-2G (Fig. 7d) whose Stage 2 phase assemblage (e.g. kyanite) records minimal replacement by Stage 3 minerals. In other matrix samples, however, moderate to advanced imprints of Stage 3 masked this leaching signature as gains in fluid mobile elements/components K_2O, Rb, and Ba (Fig. 11e). This is supported by the increase in the concentration of these elements/components in matrix samples (e.g. D113-21; Figs. 4n–o, 7f) with higher degree of Stage 3 replacement (especially muscovite) compared to other samples which preserved their Stage 2 mineral assemblages. This is consistent with the strong correlation between the K_2O, Rb and Ba contents of the matrix samples with one another but not with other fluid-mobile elements (e.g. CaO and SiO_2; Fig. 10a). These lines of evidence suggest a later fluid infiltration event related to the retrograde metamorphism of the Dalrymple Amphibolite as the mélange sequence was being exhumed towards the surface (Fig. 12a). Valera et al. (2021) described low-salinity aqueous fluid inclusions related to the growth of kyanite-replacing muscovite. The gains associated with Stage 3 minerals are also much more variable, i.e. $\Delta C_a^i / C_0^i$ = 0 to +3.29 for K_2O, compared to the losses due to early fluid-infiltration. This possibly reflect the limited nature of this retrograde event as evidenced by the variable degree of replacement in the matrix samples (e.g. kyanite by muscovite).

7.4 Assessing Mixing, fluid Infiltration, Leaching, and Deformation (MILD) processes in the slab-mantle wedge interface

In the calculations presented above, a single metasedimentary and metamafic end-member were used to reproduce the modelled composition of all matrix samples. However, in an actively deforming

765 shear zone, an end-member (e.g. metamafic) can be added into the mixing zone incrementally as distinct
766 "batches" instead of being consumed in a single deformation event. Looking at the whole rock composition
767 of the matrix samples allowed the evaluation of mechanical mixing between end-member components but
768 masked the finer details of how such a process progressed. The product of initial stages of mixing, i.e. a
769 hybridized matrix, can also be recycled and used as raw material to be deformed, mixed, and reacted with
770 infiltrating fluids (Fig. 12d). This scenario is supported by the two distinct generations of matrix observed
771 in Botoon and Nanad where the earlier formed matrix2a are transformed into blocks themselves and
772 surrounded by matrix2b. In the mixing-isocon analyses done for the Grt amphibolite block B213-9 (Fig.
773 2c–f), the use of the surrounding matrix (B213-7) and the core of the block (B213-8) largely reproduced
774 its whole rock composition aside from losses in more fluid mobile elements/components (e.g. K_2O, P_2O_5,
775 and Rb). These preferential losses in fluid-mobile elements/components from the margin of the blocks are
776 likely related to leaching by infiltration of fluids.

777 Accounting the contributions of deformation, mixing, and fluid-rock interaction in the slab-mantle
778 wedge interface is therefore complicated by its cyclical feedback nature. The procedure outlined in this
779 study, while simplistic, is thus meant to provide a workflow in the study of matrix formation in slab-mantle
780 wedge interface localities especially those dominated by mafic and sedimentary end-members. Indeed,
781 future works gathering more block and matrix samples and employing other geochemical techniques (e.g.
782 stable isotope geochemistry) are expected to refine end-member identification and estimation of mixing
783 ratios, albeit still as a cumulative and not incremental effect. More importantly, the notable consistency
784 between the interpretations for the matrix petrogenesis (i.e. mixing-leaching) and its petrological
785 characteristics (i.e. phase assemblage), whole rock data (measured vis-à-vis modelled), and mineral
786 chemistry (e.g. Nb-Cr contents of rutile) give merit to the procedural workflow employed in this study.
787 Application of this procedure to other slab-mantle wedge localities may help in distinguishing end-
788 member components, estimating their mixing ratios, and determining the effects of infiltrating fluids.

789 7.5 MILD processes in slab-mantle wedge interfaces and its implications for arc magmatism

790 The cooler paleogeothermal gradient preserved in the Dalrymple Amphibolite compared to typical
791 metamorphic soles (e.g. Semail Ophiolite; Soret et al., 2017) suggests that it represents the slab-mantle
792 wedge interface of an arc already in transition from the much warmer conditions during subduction
793 initiation (Valera et al., 2021; Fig. 12a,b). The mixing process between metasedimentary-metamafic end-
794 members observed in the Dalrymple Amphibolite also differs from what is typically observed in high-*P/T*
795 type metamorphic terranes thought to dominate developed subduction zones (Bebout and Penniston-
796 Dorland, 2016; Agard et al., 2018). In such environments, the colder and wetter conditions allow the
797 prevalence of lower-*T* phases such as serpentine and chlorite derived from the ultramafic end-member, i.e.
798 serpentinized mantle wedge (e.g. Guillot et al., 2009). Recent studies dealing with the petrogenesis of the
799 surrounding matrix in slab-mantle wedge interface complexes (e.g. Gorman et al., 2019) mainly utilized
800 stable isotopes (e.g. $^{187}Os/^{188}Os$) and highly siderophile trace elements (e.g. platinum group elements) to
801 elucidate petrogenetic processes preserved in these rocks. This procedure has been done in relatively well
802 studied localities such as the Monviso Eclogite in western Alps (e.g. Angiboust et al., 2014), and the Attic-
803 Cycladic Complex in Syros, Greece (Gorman et al., 2019). Although most high-*P*/*T* type metamorphic
804 terranes do preserve an ultramafic-derived matrix, this does not fully encapsulate other possible mixing
805 scenarios in the slab-mantle wedge interface.

806 Empirical (Nielsen and Marschall, 2017) and experimental (Codillo et al., 2018) analyses of global
807 arc lavas, clearly show the important role of the crustal section (i.e. sediments and mafic lavas) of the
808 down-going slab to account for variations in the arc magma chemistry. Early stages of subduction
809 characterized by warmer geothermal gradients than what is observed in developed arcs and early
810 dehydration at shallower depths, limit the formation of low-*T* phases such as serpentine and chlorite along
811 the slab-mantle wedge interface of an incipient arc. Indeed, these common matrix-forming minerals
812 (chlorite, serpentine, and talc) are only stable in mature arcs characterized by high-*P/T* metamorphic field
813 gradients (Agard et al., 2016).

If the serpentinization of the overlying mantle wedge is not pervasive, deformation along the slab-mantle wedge interface is likely accommodated by the crustal section of the down-going slab (e.g. Agard et al., 2016; Valera et al., 2021). Observations of metamorphic soles in some ophiolites (e.g. Semail Ophiolite) show that in such scenarios, shearing is accommodated by the deformation of rheologically weaker sediments (e.g. Soret et al., 2017). The chemistry of the matrix comprising the subduction channel during incipient subduction will therefore represent the mixture of crustal components while the contribution of the ultramafic end-member will likely be minimal (Fig. 12c). The type of end-members constituting the matrix of the Dalrymple Amphibolite and the high metased1: metamafic2A/EA ratio support such scenario.

The petrological characteristics of the matrix surrounding the blocks of the Dalrymple Amphibolite thus provide a unique perspective on sediment- and mafic-dominated slab-mantle wedge interface. Based on the characteristics of the matrix of this mélange sequence, relatively stiff minerals such as kyanite, Ca-amphibole, and garnet are more prevalent than softer, more magnesian minerals i.e. serpentine, talc and chlorite. A similar observation was noted for the matrix surrounding the amphibolite blocks of Catalina Schist (Penniston-Dorland et al., 2018). The mixing between sediment and mafic end-members also has implications on the elements that are retained and those that are mobilized during the interaction of such hybridized matrix with infiltrating fluids.

In the case of the Dalrymple Amphibolite, fluid infiltration at relatively high *P-T* conditions (~700 °C; 13 kbar) at relatively shallow depths (~45 km) resulted in the preferential leaching of fluid mobile elements/components (e.g. SiO_2, Na_2O, K_2O, Ba) while more immobile elements/components are retained (e.g. Al_2O_3, Zr, Th) and enriched in the matrix. As these fluids ascend towards shallower depths, they will likely interact and react with the mantle wedge lithologies in the hanging wall. It must be noted however, that this study deals with processes occurring at relatively shallower depths (~45 km) beneath an incipient arc with a high paleogeothermal gradient (~16 °C/km). The generally cooler geothermal

838 gradients in more developed arcs may result to deeper depths of devolatilization and therefore different
839 fluid properties and composition (e.g. Manning and Frezzotti, 2020). The local temperature-depth structure
840 of the subduction system for example may affect the preferential stabilization of certain sink minerals and
841 thus affect which elements are leached out and which are retained as was shown for the Dalrymple
842 Amphibolite. Considering these caveats, the interaction between fluids similar to what is reported here
843 and the overlying mantle material may explain, at least in part, signatures observed in arc volcanic rocks
844 and subarc mantle xenoliths.

845 Ba-enriched, Th-depleted fluids were likely produced during the leaching process of the matrix in
846 the Dalrymple Amphibolite. A fluid of this composition interacting with the mantle wedge may explain
847 the Ba-rich, Th-poor 'shallow subduction component' found in most arcs (e.g. Elliot et al., 2003; Pearce
848 et al., 2005; Manning and Frezzotti, 2020). These shallow subduction components are thought to be
849 transported by dilute, aqueous fluids released from the downgoing slab during metamorphic
850 devolatilization at depths of around ~20–70 km, depending on the local *P/T* gradient (e.g. Manning and
851 Frezzotti, 2020). Retention and enrichment of Th in the matrix of the Dalrymple Amphibolite after
852 leaching on the other hand, ensures its availability during melting and/or devolatilization of the slab at
853 deeper levels (>90 kms, Manning and Frezzotti, 2020). Melt and/or fluid derived from this Th-rich matrix
854 material, considering that Th-sink minerals are stabilized, could explain the Th-enriched 'deep (>90 km)
855 subduction component' also reported in most arcs (e.g. Elliot et al., 2003). A more direct evidence of the
856 interaction between the mantle wedge and percolating Si- and Na-rich hydrous fluids has also been
857 documented in a number of subarc xenolith localities (e.g. Western Pacific arcs; Arai and Ishimaru, 2008).
858 Silica enrichment is typically observed as the growth of secondary orthopyroxenes at the expense of
859 olivine (e.g. Batanes; Valera et al., 2019) while the crystallization of hydrous minerals such as phlogopite
860 and/or pargasite in mantle wedge xenoliths (e.g. Pinatubo; Payot et al., 2018) attests to the interaction of
861 percolating cation-rich hydrous fluids with mantle wedge lithologies albeit at deeper depths than those in
862 this study (~45 km).

8 Conclusions

The protolith of the metamafic blocks and the petrogenetic processes preserved in the matrix which comprise the Dalrymple Amphibolite are elucidated. The metamafic blocks are possibly genetically related to the basalts and gabbros comprising the crustal section of Palawan Ophiolite. The metamafic blocks represent the metamorphosed crustal section of the subducting slab, while the Palawan Ophiolite basalts constitute the unmetamorphosed crustal section of the hanging wall. Both mafic lithologies indicate a MORB signature.

The matrix surrounding the blocks reflects the complex interplay of deformation in this shear zone, mixing of mafic and sedimentary crustal components, and leaching and addition of elements by different generations of infiltrating fluids. Our results indicate the predominant effect of mixing between metamafic and metasedimentary components in controlling its major and trace element contents. The crustal end-members identified for the matrix of the Dalrymple Amphibolite with its intermediate paleogeothermal gradient (~16 °C/km) contrast with typical high-*P*/*T* type metamorphic terranes which feature a hybrid matrix derived from mixed ultramafic-sedimentary units.

A fluid infiltration event likely occurred during the deformation and mixing of crustal components in the shear zone. This event resulted in the preferential leaching not only of fluid mobile components (e.g. CaO and SiO_2) but also other elements/components not utilized by the crystallizing minerals in the matrix. A subsequent fluid infiltration event related to the retrogression of the Dalrymple Amphibolite resulted in the addition of K_2O, Rb, and Ba in the whole rock composition of the matrix as replacive minerals (e.g. muscovite).

Similar mixing, deformation, and fluid-related mass transfer processes likely operate in other slab-mantle wedge interface localities and actively control the petrological and geochemical signatures of the matrix of these mélange sequences. Fluids infiltrating and interacting with this hybridized matrix material, in particular, may preferentially leach some elements and retain and enrich others depending on the stable phase assemblage in the matrix, thus gaining distinct geochemical signatures. As these fluids rise along

the slab-mantle wedge interface and react with the overlying mantle material, some of these distinct signatures may be imprinted on the mantle wedge and consequently affect arc magma chemistry.

ACKNOWLEDGEMENTS

We acknowledge the logistical support provided by the Rushurgent Working Group of the University of the Philippines Diliman, the Palawan Council for Sustainable Development (PCSD) and the local government units (LGUs) of Puerto Princesa, Palawan (SEP Clearance UAC-011519-024) during our fieldwork. M. Takaya of Kyoto University is thanked for the preparation of thin sections. Valuable discussions with T. Hirajima and K. Naemura are also appreciated. This work forms part of the doctoral thesis of the first author under the Japanese Government (Monbukagakusho) scholarship program. This work was supported by the JSPS KAKENHI Grant Number JP19H01991 of the second author, and a research grant from the National Research Council of the Philippines (NRCP P-028) of the third author. Comments from two anonymous reviewers helped improve the initial version of this manuscript. Editorial handling and comments by Prof. B. Kamber is also highly appreciated.

REFERENCES

Agard, P., Plunder, A., Angiboust, S., Bonnet, G., Ruh, J., 2018. The subduction plate interface: Rock record and mechanical coupling (from long to short timescales). Lithos 320–321, 537–566.

Agard, P., Yamato, P., Soret, M., Pringent, C., Guillot, S., Plunder, A., Dubacq, B., Chauvet, A., Monie, P., 2016. Plate interface rheological switches during subduction infancy: Control on slab penetration and metamorphic sole formation. Earth and Planetary Science Letters 451, 208–220.

Angel, R.J., Mazzuccheli, M.L., Alvaro, M., Nestola, F., 2017. EoSFit-Pinc: A simple GUI for host-inclusion elastic thermobarometry. American Mineralogist 102, 1957–1960.

Angiboust, S., Pettke T., Hoog, J.C.M., Caron, B., Oncken, O., 2014. Channelized fluid flow and eclogite-facies metasomatism along the subduction shear zone. Journal of Petrology 55, 883–916.

Arai, S., Ishimaru, S., 2008. Insights into petrological characteristics of the lithosphere of mantle wedge beneath arcs through peridotite xenoliths: A review. Journal of Petrology 49, 665–695.

914 Bebout, G.E., 2013. Metasomatism in subduction zones of subduction zones of subducted oceanic slabs,
915 mantle wedges, and the slab-mantle interface In: Harlov, D.E., Austrheim, H. Metasomatism (eds.)
916 Metasomatism and the chemical transformation of rock. Lecture notes in Earth system sciences,
917 Springer-Verlag Berlin Heidelberg, 289–349.

918 Bebout, G.E., Barton, M.D., 2002. Tectonic and metasomatic mixing in a High-T, subduction-zone
919 melange – Insights into the geochemical evolution of the slab-mantle interface. Chemical Geology
920 187, 79–106.

921 Bebout, G.E., Penniston-Dorland, S.C., 2016. Fluid and mass transfer at subduction interfaces - The field
922 metamorphic record. Lithos 240–243, 228–258.

923 Codillo, E.A., Le Roux, V., Marschall, H.R., 2018. Arc-like magmas generated by melange-peridotite
924 interaction in the mantle wedge. Nature Communications 9, 1–11.

925 Droop, G.T.R., 1987. A general equation for estimating Fe3+ concentrations in ferromagnesian silicates
926 and oxides from microprobe analyses, using stoichiometric criteria. Mineralogical Magazine 51,
927 431–435.

928 Dycoco, J.M.A., Payot, B.D., Valera, G.T.V., Labis, F.A.C., Pasco, J.A., Perez, A.d.C., Tani, K., 2021.
929 Juxtaposition of Cenozoic and Mesozoic ophiolites in Palawan island, Philippines: New insights on
930 the evolution of the Proto-South China Sea. Tectonophysics 819, 229085.

931 Elliot, T., 2003. Tracers of the Slab. In: Eiler, J. (Ed.) Inside the subduction factory. Geophysical
932 Monograph 138, American Geophysical Union, Washington D.C. 23–45.

933 Encarnacion, J.P., Essene, E.J., Mukasa, S.B., Hall, C.H., 1995. High-pressure and -temperature
934 subophiolitic kyanite-garnet amphibolites generated during initiation of Mid-Tertiary subduction,
935 Palawan, Philippines. Journal of Petrology 36, 1481–1503.

936 Gerya T., Stöckhert, B., Perchuk, A.L., 2002. Exhumation of high-presure metamorphic rocks in a
937 subduction channel: A numerical simulation. Tectonics 21, 1–15.

938 Gibaga, C.R., Arcilla, C.A., Hoang, N., 2020. Volcanic rocks from the Central and Southern Palawan
939 Ophiolites, Philippines: Tectonic and mantle heterogeneity constraints. Journal of Asian Earth
940 Sciences: X. 4, j.jaesx.2020.100038

941 Gorman, J.K., Penniston-Dorland, S.C., Marschall, H.R., Walker, R.J., 2019. The roles of mechanical
942 mixing and fluid transport in the formation of reaction zones in subduction-related mélange:
943 Evidence from highly siderophile elements. Chemical Geology 2019, 96–111.

944 Grant, J.A.,1986. The isocon diagram – a simple solution to Gresen's equation for metasomatic alteration.
945 Economic Geology 81, 1976–1982.

946 Gresens, R.L., 1967. Composition-volume relationships of metasomatism. Chemical Geology 2, 47–65.

947 Gromet, L.P., Dymek, R.F., Haskin, L.A., Korotev, R.L., 1984. The “North American Shale Composite”:
948 its compilation, major and trace element characteristics. Geochimica et Cosmochima Acta 48,
949 2469–2482.

950 Guillot, S., Hattori, K., Agard, P., Schwartz, S., Vidal, O., 2009. Exhumation processes in oceanic and
951 continental subduction contexts: A review In: Lallemand, S., Funiciello, F. (eds.) Subduction zone
952 geodynamics. Springer-Verlag Berlin Heidelberg, 175–205.

953 Hofmann, A.W., 1988. Chemical differentiation of the Earth: The relationship between mantle, continental
954 crust and oceanic crust. Earth and Planetary Science Letters 90, 297–314.

955 Irvine, T.N., Baragar, W.R.A., 1971. A guide to the chemical classification of the common volcanic rocks.
956 Candian Journal of Earth Sciences 8, 523–548.

957 Kapp, P., Manning, C.E., Tropper, P., 2009. Phase-equilibrium constraints on titanite and rutile activities
958 in mafic epidote amphibolites and geobarometry using titanite-rutile equilibria. Journal of
959 Metamorphic Geology 27, 509–521.

960 Keenan, T.E., Encarnacion, J., Buchwaldt, R., Fernandez, D., Mattinson, J., Rasoazanamparany, C.,
961 Leutkemeyer, P.B., 2016. Rapid conversion of an oceanic spreading center to a subduction zone
962 inferred from high-precision geochronology. Proceedings of the National Academy of Sciences 113,
963 E7359–E7366.

964 Kelemen, P.B., Koga, K., Shimizu, N., 1997. Geochemistry of gabbro sills in the crust-mantle transition
965 zone of the Oman ophiolite: Implications for the origin of the oceanic lower crust. Earth and
966 Planetary Science Letters 146, 475–488.

967 Labis, F.A.C., Payot, B.D., Valera, G.T.V., Pasco, J.A., Dycoco, J.M.A., Tamura, A., Morishita, T., Arai,
968 S., 2020. Melt-rock interaction in the subarc mantle: Records from the plagioclase peridotites of
969 the southern Palawan Ophiolite, Philippines. International Geology Review 63, 1067–1089.

970 Leake, B.E., Woolley, A.R., Arps, C.E.S., Birch, W.D., Gilbert, M.C., Grice, J.D., Hawthorne, F.C., Kato,
971 A., Kisch, H.J., Krivovichev, V., Linthout, K., Laird, J., Mandarino, J.A., Maresch, W.V., Nickel,
972 E.H., Rock, N.M.S., Schumacher, J.C., Smith, D.C., Stephenson, N.C.N., Ungaretti, L., Whittaker,
973 E.J.W., Youzhi, G., 1997. Nomenclature of amphiboles: Report of the subcommittee on amphiboles
974 of the international mineralogical association, commission on new minerals and mineral names.
975 The Canadian Mineralogist 35, 219–246.

976 Li, C.F., Xu, X., Lin, J., Sun, Z., Zhu, J., Yao, Y.J., Zhao, X.X., Liu, Q.S., Kulhanek, D.K.,Wang, J., Song,
977 T.R., Zhao, J.F., Qiu, N., Guan, Y., Zhou, Z., Williams, T., Bao, R., Briais, A., Brown, E., Chen,
978 Y., Clift, P., Colwell., F., Dadd, K., Ding, W., Almeida, I., Huang, X., Hyun, S., Jiang, T., Koppers,
979 A., Li, Q., Liu, C., Liu, Z., Nagai, R., Peleo-Alampay, A., Su, X., Tejada, M., Trinh, H., Yeh, Y.,
980 Zhang, C., Zhang, F., Zhang, G., 2014. Ages and magnetic structures of the South China Sea
981 constrained by deep tow magnetic surveys and IODP Expedition 349. Geochemistry, Geophysics,
982 Geosystems 15, 4958–4983.

983 Lopez-Moro, F.J., 2012. EASYGRESGRANT – A Microsoft Excel spreadsheet to quantify volume
984 changes and to perform mass-balance modeling in metasomatic systems. Computer and
985 Geosciences 39, 191–196.

986 Manning, C.E., Frezzotti, M.L., 2020. Subduction-zone fluids. Elements 16, 395–400.

987 Marschall, H.R., Schumacher, J.C., 2012. Arc magmas sourced from melange diapirs in subduction zones.
988 Nature Geoscience 5, 862–867.

989 Meinhold, G., Anders, B., Kostopoulos, D., Reischmann, T., 2008. Rutile chemistry and thermometry as
990 provenance indicator: An example from Chios Island, Greece. Sedimentary Geology 203, 98–111.

991 Nakashima, T., Shimoda, G., Tatsumi, Y., 2000. Porphyritic magnesian andesites in the Setouchi Volcanic
992 Belt, SW Japan. Bulletin of the Volcanological Society of Japan 45, 259–269.

993 Nielsen, S.G., Marschall, H.R., 2017. Geochemical evidence for mélange melting in global arcs. Science
994 Advances 3:e1602402, 1–6.

995 Payot, B.D., Arai., S., Yoshikawa, M., Tamura, A., Okuno, M., Rivera, D.J.V., 2018. Mantle evolution
996 from ocean to arc: The record in spinel peridotite xenoliths in Mt. Pinatubo, Philippines. Minerals
997 8, 1–16. Doi: 10.3390/min8110515.

998 Peacock, S., Wang, K., 1999. Seismic consequences of warm versus cool subduction metamorphism:
999 Examples from Southwest and Northeast Japan. Science 286, 937–939.

1000 Pearce, J.A., Cann, J.R., 1971. Ophiolite origin investigated by discriminant analysis using Ti, Zr, and Y.
1001 Earth and Planetary Science Letters 12, 339–349.

1002 Pearce, J., Stern, R., Bloomer, S., Fryer, P., 2005. Geochemical mapping of the Mariana arc-basin system:
1003 Implications for the nature and distribution of subduction components. Geochemistry, Geophysics,
1004 Geosystems 6 (2004GC000895).

1005 Penniston-Dorland, S.C., Gorman, J.K., Bebout, G.E., Piccoli, P.M., Walker, R.K., 2014. Reaction rind
1006 formation in the Catalina Schist: Deciphering a history of mechanical mixing and metasomatic
1007 alteration. Chemical Geology 384, 47–61.

1008 Penniston-Dorland, S.C., Kohn, M.J., Piccoli, P.M., 2018. A melange of subduction temperatures:
1009 Evidence from Zr-in-rutile thermometry for strengthening of the subduction interface. Earth and
1010 Planetary Science Letters 482, 525–535.

1011 Sachs, L., 1984. Applied statistics: A handbook of techniques, 2nd Ed. Spriver-Verlag, New York, 1–707.

1012 Schumacher, J.C., 1991. Empirical ferric iron corrections: Necessity, assumptions and effects on selected
1013 geothermobarometers. Mineralogical Magazine 55, 3–18.

1014 Shimoda, G., Nagai.M., Morishita, Y., 2004. Rare earth elements compositions of Setouchi high Mg
1015 andesites (HMAs) and basalt; an implication for a mantle compositional shift beneath the SW Japan
1016 arc during the Japan Sea opening. Bulletin of the Geological Survey of Japan 55, 31–38.

1017 Soret, M., Agard, P., Dubacq, B., Plunder, A., Yamato, P., 2017. Petrological evidence for stepwise
1018 accretion of metamorphic soles during subduction infancy (Semail ophiolite, Oman and UAE).
1019 Journal of Metamorphic Geology 35, 1051–1080.

1020 Starr, P.G., Pattison, D.R.M., 2019. Metamorphic devolatilization of basalts across the greenschist-
1021 amphibolite facies transition zone: Insights from isograd mapping, petrography and thermodynamic
1022 modelling. Lithos 342–343, 295–314.

1023 Tatsumi, Y., 2005. The subduction factory: How it operates in the evolving Earth. GSA Today 15,
1024 10:1130/1052-5173.

1025 Tomkins, H. S., Powell, R., Ellis, D. J., 2007. The pressure dependence of the zirconium-in-rutile
1026 thermometer. Journal of Metamorphic Geology 25, 703–713.

1027 Ulmer, P., Trommsdorff, V., 1995. Serpentine stability to mantle depths and subduction-related
1028 magmatism. Science 268, 858–861.

1029 Valera, G.T.V., Kawakami, T., Payot, B.D., 2021. The slab-mantle wedge interface of an incipient
1030 subduction zone: Insights from the P-T-D evolution and petrological characteristics of the
1031 Dalrymple Amphibolite, Palawan Ophiolite, Philippines. Journal of Metamorphic Geology. DOI:
1032 10.1111/jmg.12644, 1–33.

1033 Valera, G.T.V., Payot, B.D., Arai, S., Takeuchi, M., Ishimaru, S., Tamura A., 2019. Petrologic nature of
1034 the active subarc crust-mantle boundary: Mixed magmatic-metasomatic processes recorded in
1035 xenoliths from Sabtang island, Luzon arc. Journal of Volcanology and Geothermal Research 374,
1036 80–99.

1037 Vielzeuf, D., Schmidt, M.W., 2001. Melting relations in hydrous systems revisited: applications to
1038 metapelites, metagreywackes and metabasalts. Contributions to Mineralogy and Petrology 141,
1039 251-267.

1040 Whitney, D.L., Evans, B.W., 2010. Abbreviations for names of rock-forming minerals. American
1041 Mineralogist 95, 185–187.

1042 Yumul, G.P.Jr., Dimalanta, C.B., Gabo-Ratio, J.A.S., Queaño, K.L., Armada, L.T., Padrones, J.T.,
1043 Faustino-Eslava, D.V., Payot, B.D., Marquez, E.J., 2020. Mesozoic rock suites along western
1044 Philippines: Exposed proto-South China Sea fragments? Journal of Asian Earth Sciences: X 4,
1045 100031.

1046 Zack, T., Moraes, R., Kronz, A., 2004. Temperature dependence of Zr in rutile: Empirical calibration of a
1047 rutile thermometer. Contributions to Mineralogy and Petrology 148, 471–488.

1048

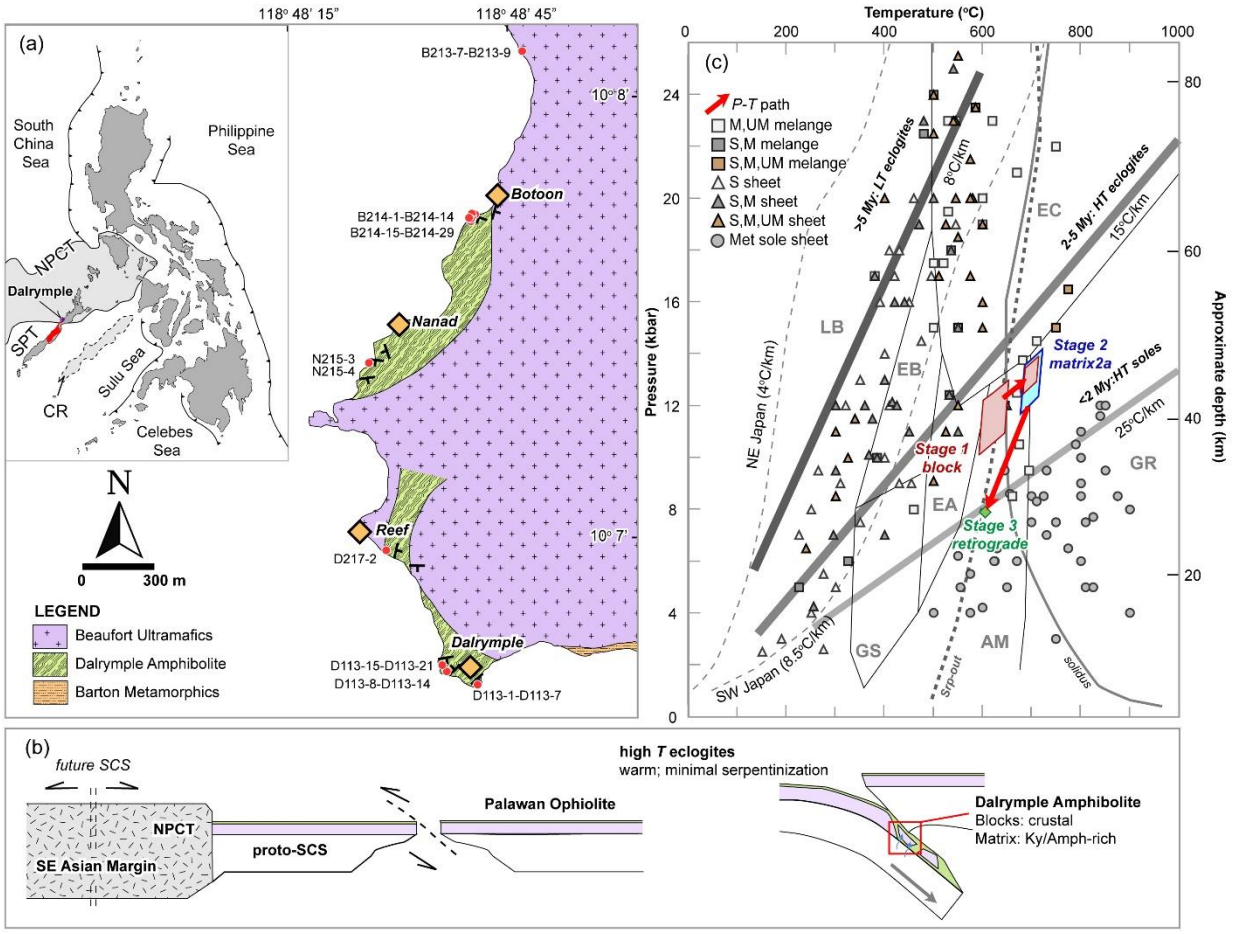

Fig. 1a) Map showing the distribution of the Dalrymple Amphibolite of the central Palawan Ophiolite (red fill in inset map) in Ulugan Bay. Inset map shows tectonic map of the Philippines, the surrounding marginal basins and trenches. NPCT-North Palawan Continental Terrane, SPT-South Palawan Terrane, CR-Cagayan de Sulu Ridge. Modified from Labis et al. (2020); b) Schematic representation of the subduction initiation of the proto-South China Sea (SCS) during the opening of the South China Sea (future SCS). c) *P-T* estimates for the Grt amphibolite block (Stage 1), matrix 2a (Stage 2) and retrograde metamorphism (Stage 3) of the Dalrymple Amphibolite adopted from Valera et al. (2021). Also shown are *P-T* conditions of metamorphic soles (Met sole sheet) and other slab-mantle wedge interfaces (sheets and melanges) compiled from Agard et al. (2016) and Agard et al. (2018). M-mafic, UM-ultramafic, S-sedimentary. Metamorphic facies (Guillot et al., 2009): LB-lawsonite blueschist, EB-epidote blueschist, EC-eclogite, GS-greenschist, EA-epidote amphibolite, AM-amphibolite, GR-granulite. Water-saturated solidus curve for MOR basalt from Vielzeuf and Schmidt (2001). Srp-out curve is from Ulmer and Trommsdorff (1995). Geothermal gradients of hot (SW Japan) and cold (NE Japan) subduction zones are from Peacock and Wang (1999).

1049

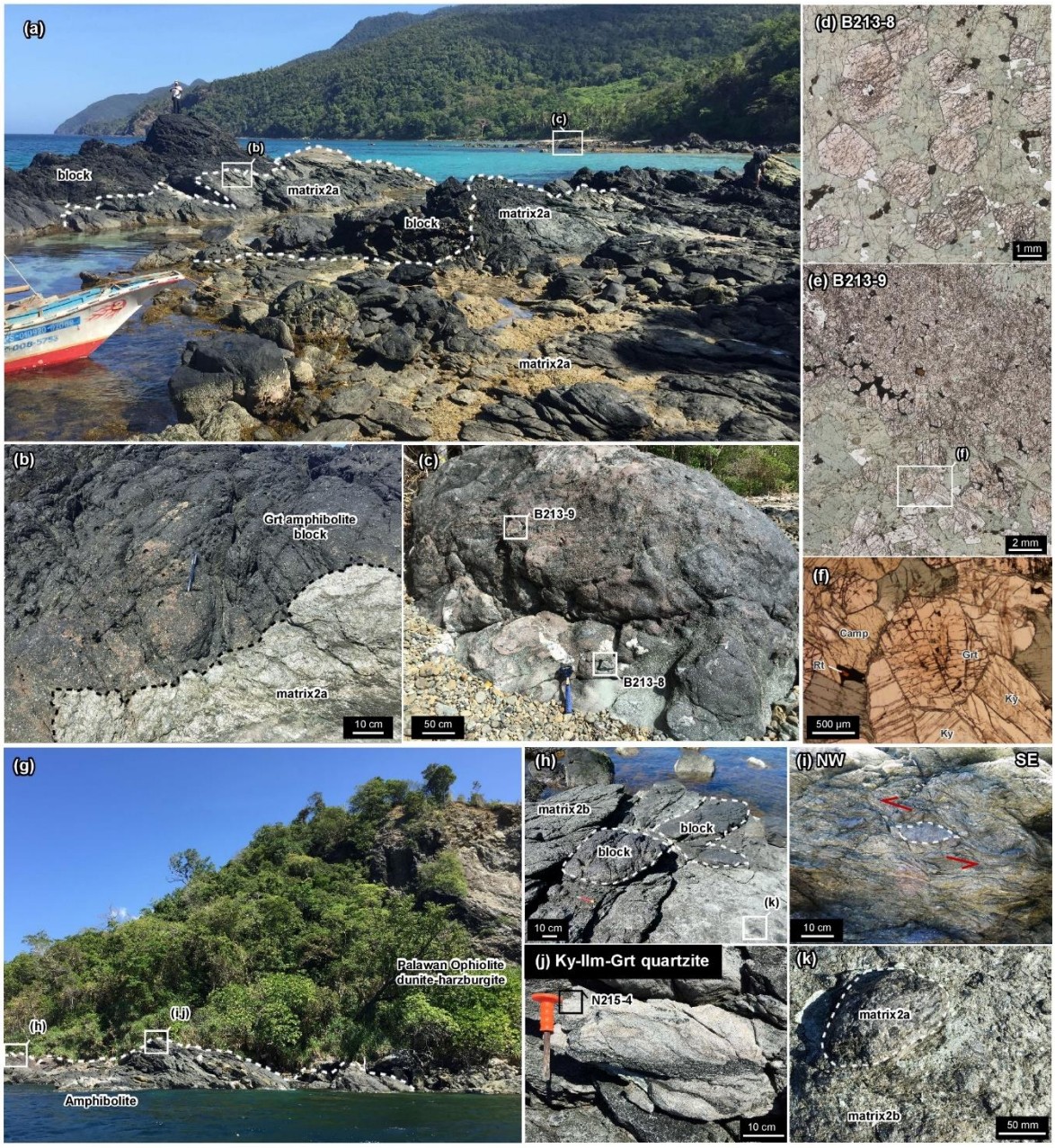

Fig. 2. a-f) Field photos of the exposure in Botoon and g-k) Nanad. a-b) photo of the block-in-matrix sequence. The boundary between block and matrix are outlined by the dashed line. c) Block in Botoon with d) Kyanite-free core portion (B213-8) and e-f) Kyanite-bearing sample (B213-9) at the edge of the block. Photomicrograph in d-f are in plane-polarized light. g) Interlayers of dunite and harzburgite thrusted on top of the Dalrymple Amphibolite. h) The exposure in Nanad exhibits the same block-in-matrix fabric observed in Botoon but have smaller blocks with more rounded edges. i) Deformed amphibolite block indicating a top to the NW sense of shear. j) The blocks in Nanad also include quartzites as well as k) Earlier formed matrix2a surrounded by a highly sheared matrix2b.

1050

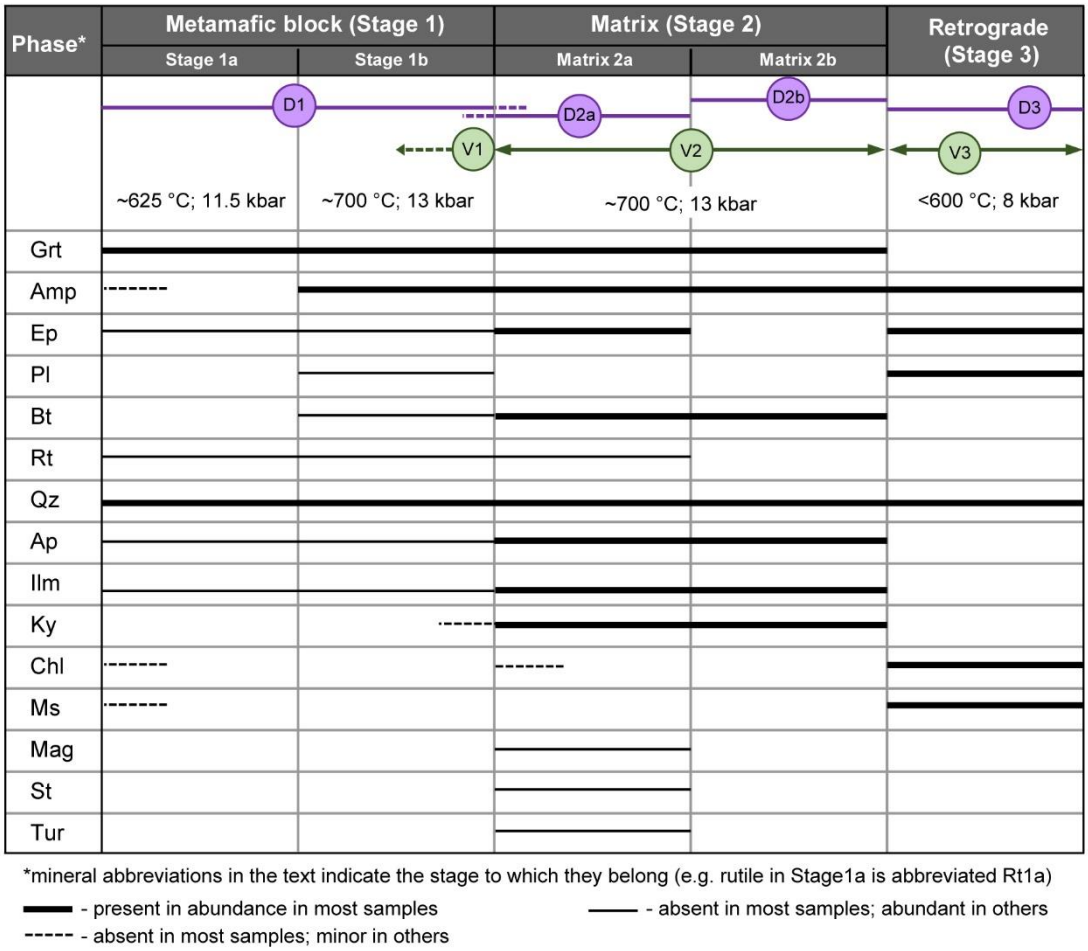

Fig. 3. Summary of the mineral paragenesis comprising the block (Stage 1), matrix (Stage 2), and replacement minerals (Stage 3) adopted from Valera et al. (2021). The deformation (D) and veining (V) stages of the Dalrymple Amphibolite are also indicated. The *P*-*T* conditions for each stage are also shown.

1051

1052

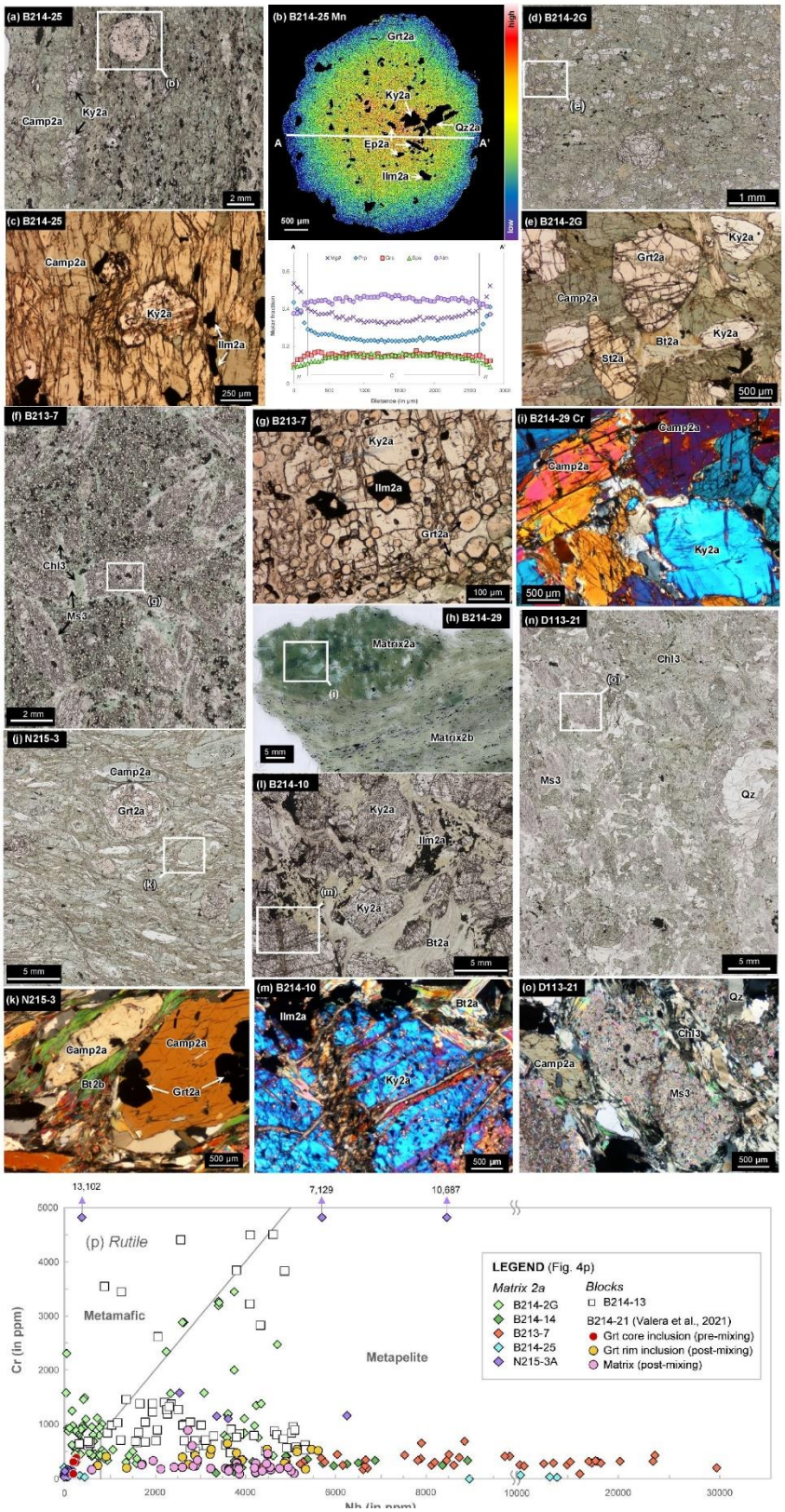
(a) B214-25
(b)
Camp2a
Ky2a
2 mm
(b) B214-25 Mn
Grt2a
Ky2a
Qz2a
A
A'
Ep2a
Ilm2a
500 µm
high
low
(d) B214-2G
(e)
1 mm
(c) B214-25
Camp2a
Ky2a
Ilm2a
250 µm
(e) B214-2G
Ky2a
Grt2a
Camp2a
Bt2a
Ky2a
St2a
500 µm
(f) B213-7
Chl3
(g)
Ms3
2 mm
(g) B213-7
Ky2a
Ilm2a
Grt2a
100 µm
(i) B214-29 Cr
Camp2a
Camp2a
Ky2a
500 µm
(h) B214-29
Matrix2a
(i)
Matrix2b
5 mm
(n) D113-21
Chl3
(o)
Ms3
Qz
5 mm
(j) N215-3
Camp2a
Grt2a
(k)
5 mm
(l) B214-10
Ky2a
Ilm2a
(m)
Ky2a
Bt2a
5 mm
(k) N215-3
Gamp2a
Camp2a
Bt2b
Grt2a
500 µm
(m) B214-10
Ilm2a
Bt2a
Ky2a
500 µm
(o) D113-21
Qz
Chl3
Camp2a
Ms3
500 µm
13,102
7,129
10,687
(p) Rutile
Metamafic
Metapelite
Cr (in ppm)
Nb (in ppm)
LEGEND (Fig. 4p)
Matrix 2a
B214-2G
B214-14
B213-7
B214-25
N215-3A
Blocks
B214-13
B214-21 (Valera et al., 2021)
Grt core inclusion (pre-mixing)
Grt rim inclusion (post-mixing)
Matrix (post-mixing)

1053

Fig. 4. Photomicrographs and compositional map of matrix samples. a) Hornblende-rich sample B214-25 which contain b) Coarse garnet with subtle prograde zonation in contrast to the pronounced zonation in garnet amphibolite blocks (Valera et al., 2021). c) Kyanite (Ky2a) in the matrix in textural equilibrium with hornblende (Camp2a) and ilmenite (Ilm2a). d) Aluminosilicate-rich matrix sample B214-2G where e) Garnet (Grt2a), kyanite (Ky2a), and staurolite (St2a) coexist with hornblende and biotite (Bt2a). f) Hornblende-free, garnet-rich matrix sample B213-7 composed exclusively of g) kyanite, fine euhedral garnet and ilmenite. Surrounding these Stage 2 minerals are replacement phases such as chlorite (Chl3) and muscovite (Ms3). h–k) Matrix samples containing both matrix2a and matrix2b. i) B214-29 only consist of kyanite (Ky2a) and amphibole (Camp2) while k) N215-3 also contain coarse garnet porphyroclasts and finer euhedral garnet grains included in hornblende. l) Metapelitic-looking matrix sample B214-10 composed almost exclusively of m) Biotite, ilmenite, and relatively unaltered coarse kyanite. n) Hornblende-rich matrix sample D113-21, extensively affected by Stage 3 retrograde metamorphism. o) Fine muscovite pseudomorph after kyanite. All photomicrographs are in plane polarized light, except i, k, m, and o which are in crossed polarized light. p) Cr-Nb contents of rutile in matrix2a and some block samples showing mixed metapelite-metamafic signatures. Metapelite and metamafic fields are from Meinhold et al. (2008). Some metamafic blocks exhibit enriched LREEs and Th concentration and are labelled as “Sedimentary” signature. Rutile with high Nb content are also found in such samples (e.g. B214-13).

1054

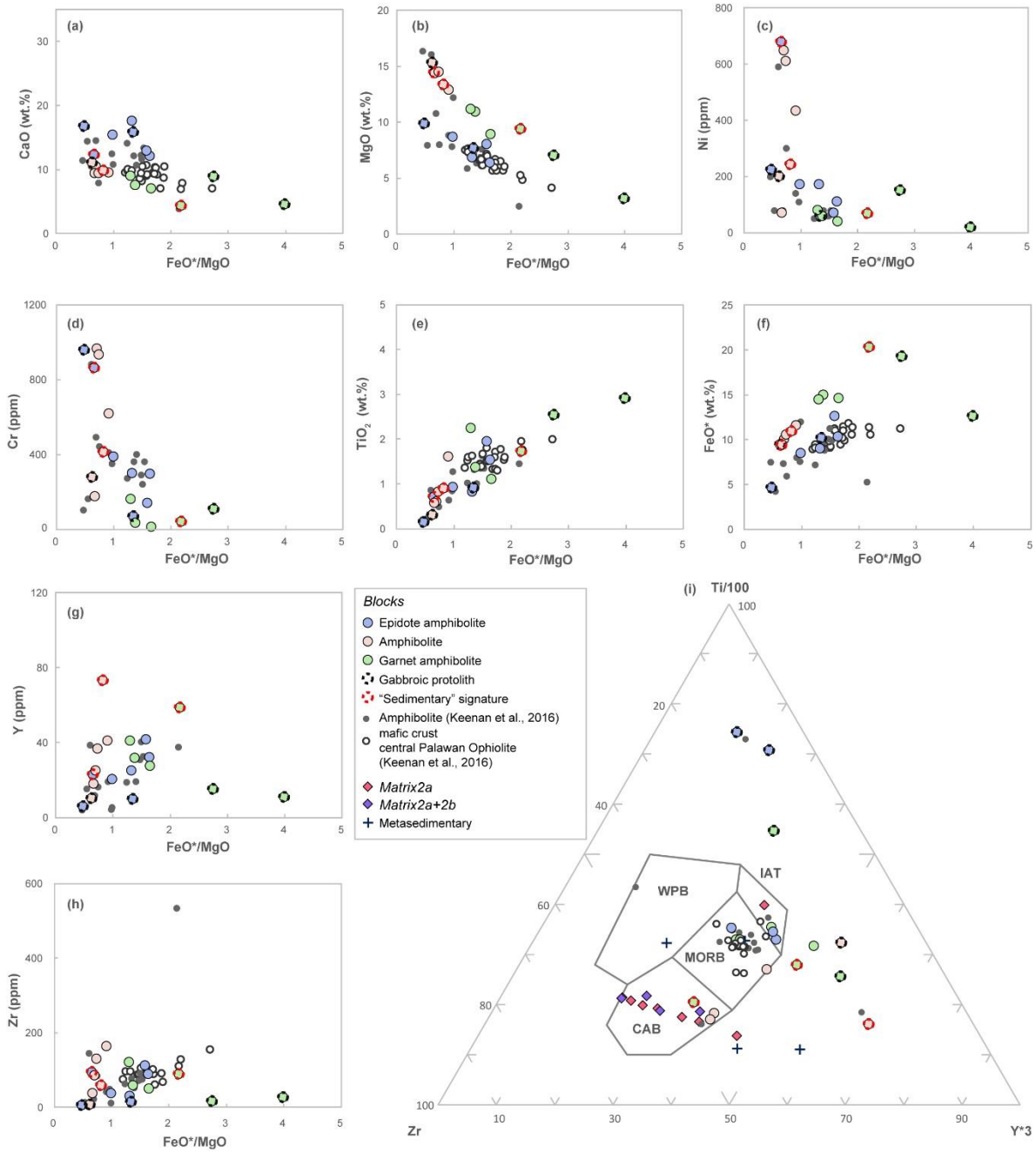

Fig. 5. a–h) Binary plots against FeO*/MgO of the mafic crust of central Palawan Ophiolite (Keenan et al., 2016) and Dalrymple Amphibolite (this study and Keenan et al., 2016). Compatible elements such as a) CaO, b) MgO, c) Ni, and d) Cr of the amphibolite and mafic crust of the central Palawan Ophiolite show decreasing trend with increasing differentiation (increasing FeO*/MgO). Tholeiitic signature is also preserved in these lithologies as increasing e) TiO_2 and f) FeO* with increasing FeO*/MgO. Incompatible elements g) Y and h) Zr show a positive slope which is consistent with magmatic differentiation trends while amphibolites derived from gabbroic cumulates recorded the lowest concentrations. See text for details. FeO* = Total Fe as FeO. i) Zr-Ti-Y tectonic discrimination diagram (after Pearce and Cann, 1971). Most amphibolite of Keenan et al. (2016) and mafic crust of the central Palawan ophiolite plot within the MORB field, while amphibolites from this study exhibit more extensive variability. Metasedimentary blocks and matrix samples have distinctly higher Zr content. The fields are as follows: IAT – island arc tholeiites, WPB – within plate basalts, MORB – mid oceanic ridge basalts and CAB – calc-alkaline basalts.

1055

1056

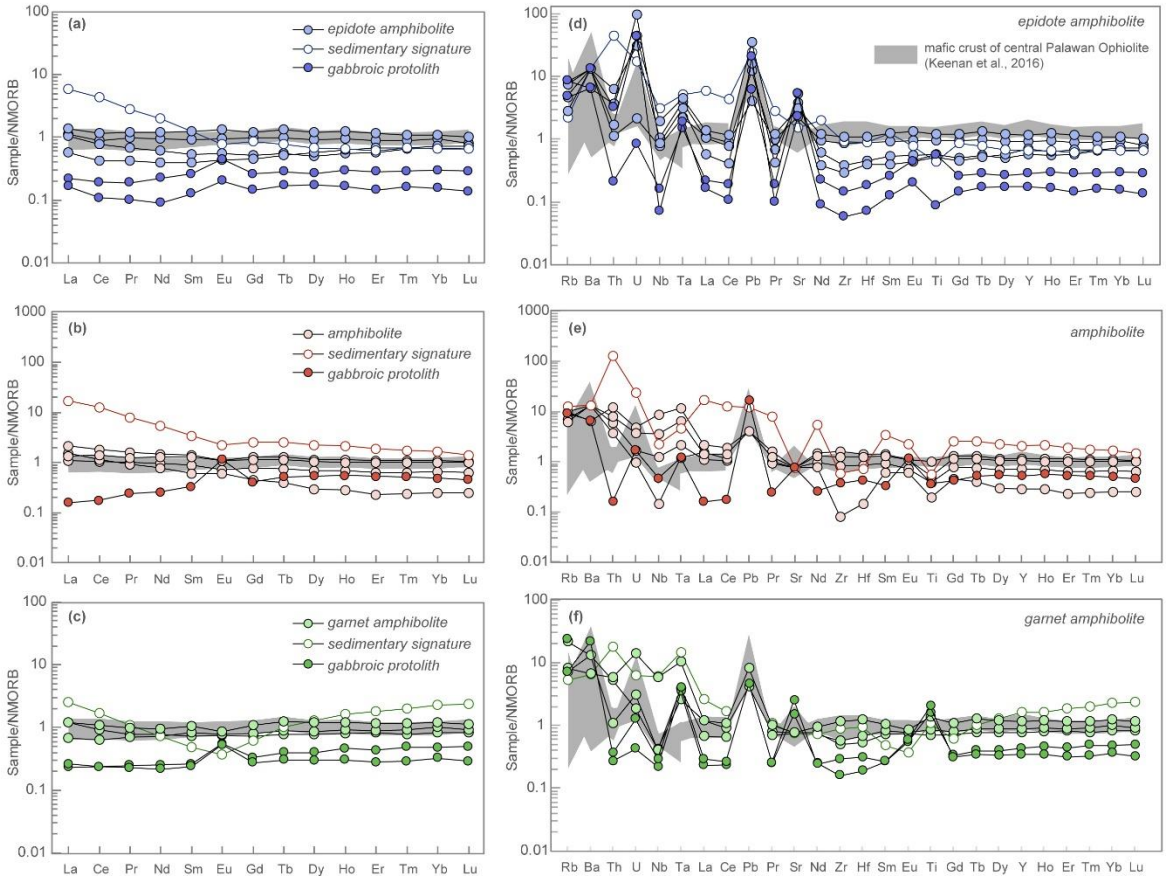

Fig. 6. Trace element data of the metamafic blocks. a–c are normal mid-oceanic ridge basalt (NMORB)-normalized rare earth element (REE) plots of a) epidote amphibolite b) amphibolite, and c) garnet amphibolite blocks of the Dalrymple Amphibolite. Fig. d–f are NMORB-normalized extended trace element diagram of d) epidote amphibolite, e) amphibolite and f) garnet amphibolite blocks. Shown as open symbols are samples with sedimentary signature while darker shades are used for amphibolite blocks derived from a gabbroic protolith (see text for details). Also shown as grey fields are the data for the mafic crust of central Palawan Ophiolite from Keenan et al. (2016).

1057

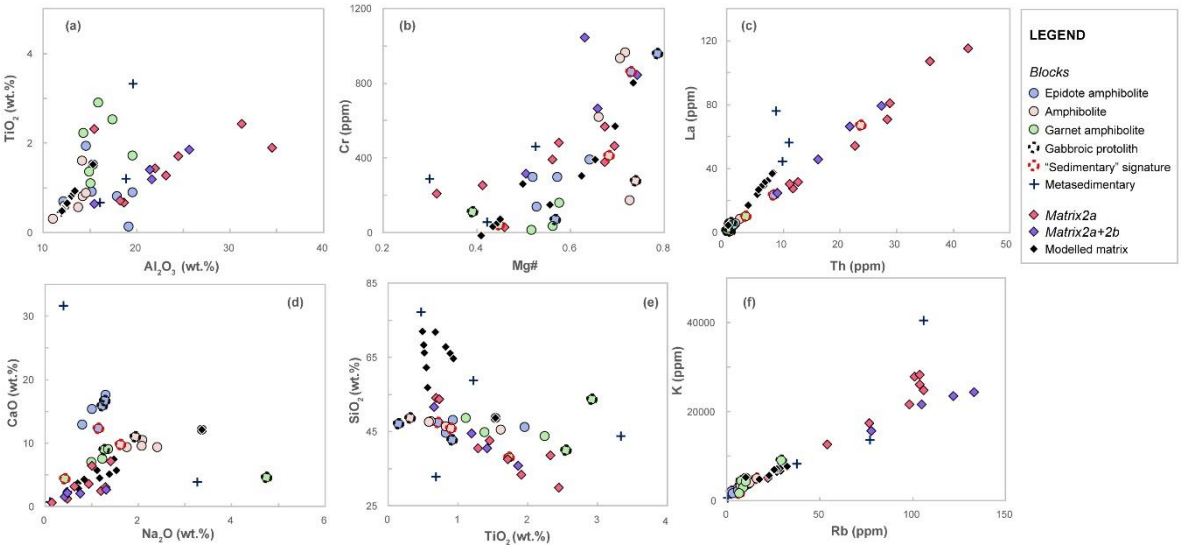

Fig. 7. a–f) binary plots of whole rock composition of matrix and block samples. The modelled matrix composition is also shown as black diamonds. a) The matrix samples show positive correlation in their Al_2O_3 vs. TiO_2, b) Cr vs Mg#, and c) La vs Th compositions. The measured matrix compositions have notably higher Al_2O_3, La, and Th contents compared to the modelled matrix and the block samples. d) The measured matrix compositions generally have less CaO and Na_2O compared to the metamafic blocks. e) Slight differences in major oxide contents of the two metamafic end-members (metamafic2A and 2EA) inevitably result to distinct trends for the modelled matrix. Regardless of the metamafic end-member used however, both arrays of modelled matrix compositions predict an originally higher SiO_2 content in contrast to the generally depleted SiO_2 of the measured matrix. f) The matrix samples have higher K_2O, Rb, and Ba (not shown) than the amphibolite blocks and the modelled matrix.

1058

1059

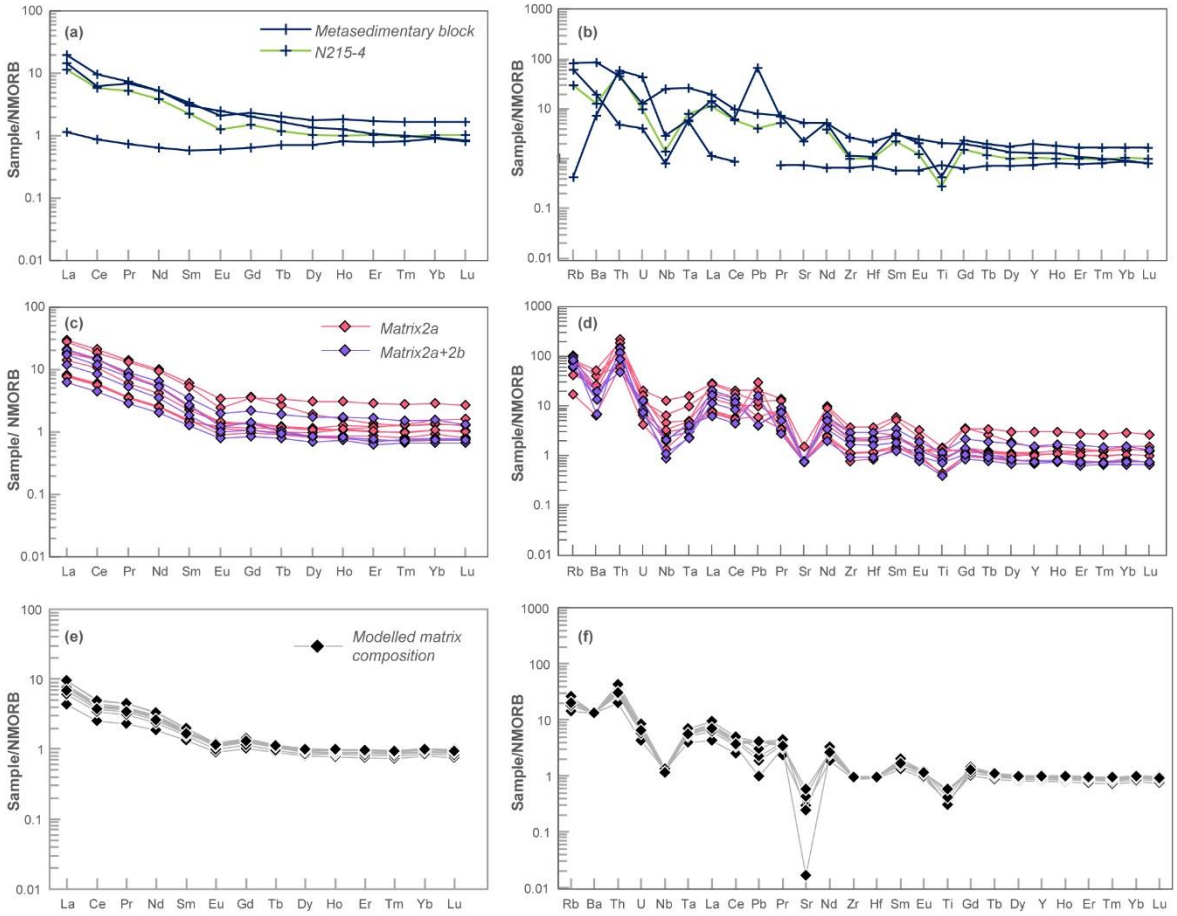

Fig. 8. a,b) NMORB-normalized REE and c,d) extended trace element plots of a,b) metasedimentary blocks, c,d) measured matrix compositions. The metasedimentary block N215-4 exhibits similar REE and trace element patterns as the matrix samples characterized by negative anomaly in Eu, Ba, Nb, Sr and Ti. The same trends are also replicated in the modelled matrix composition. e,f) REE and extended trace element plot of the modelled matrix composition.

1060

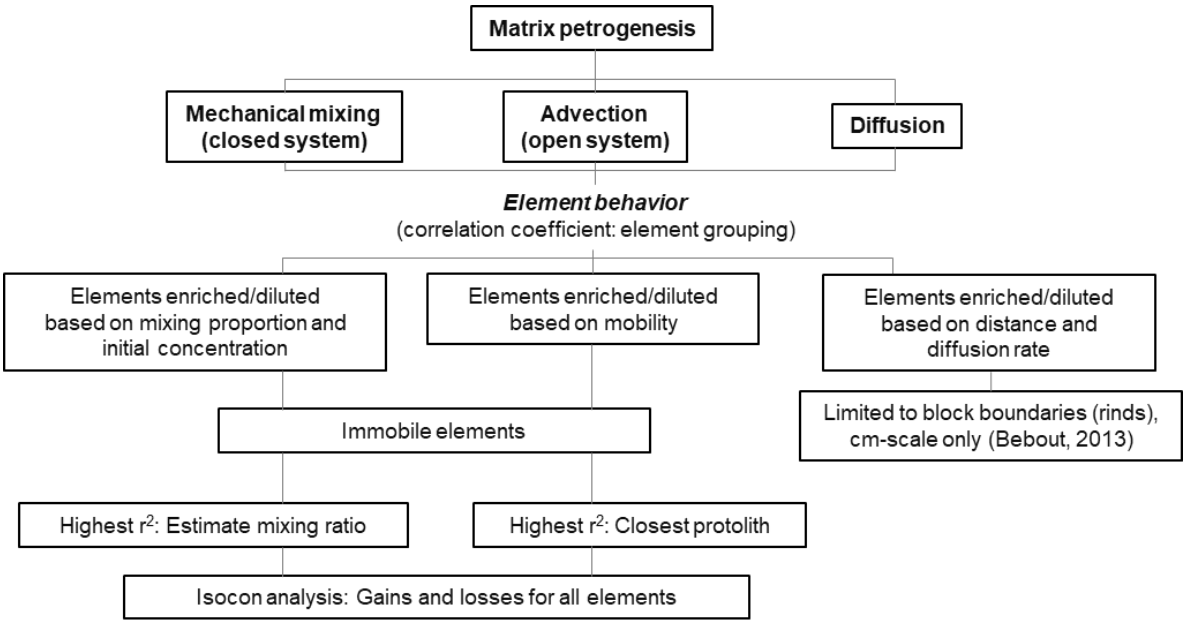

1061

Fig. 9 Schematic diagram showing the procedural work flow employed in this study to distinguish the effects of mixing and advection which may have controlled the whole rock chemistry of the matrix. Diffusion was not considered due to sampling limitations. Its effect however would likely be limited in scale (Bebout, 2013) and restricted to rind formation along block/matrix boundaries. See text for further details.

1062

1063

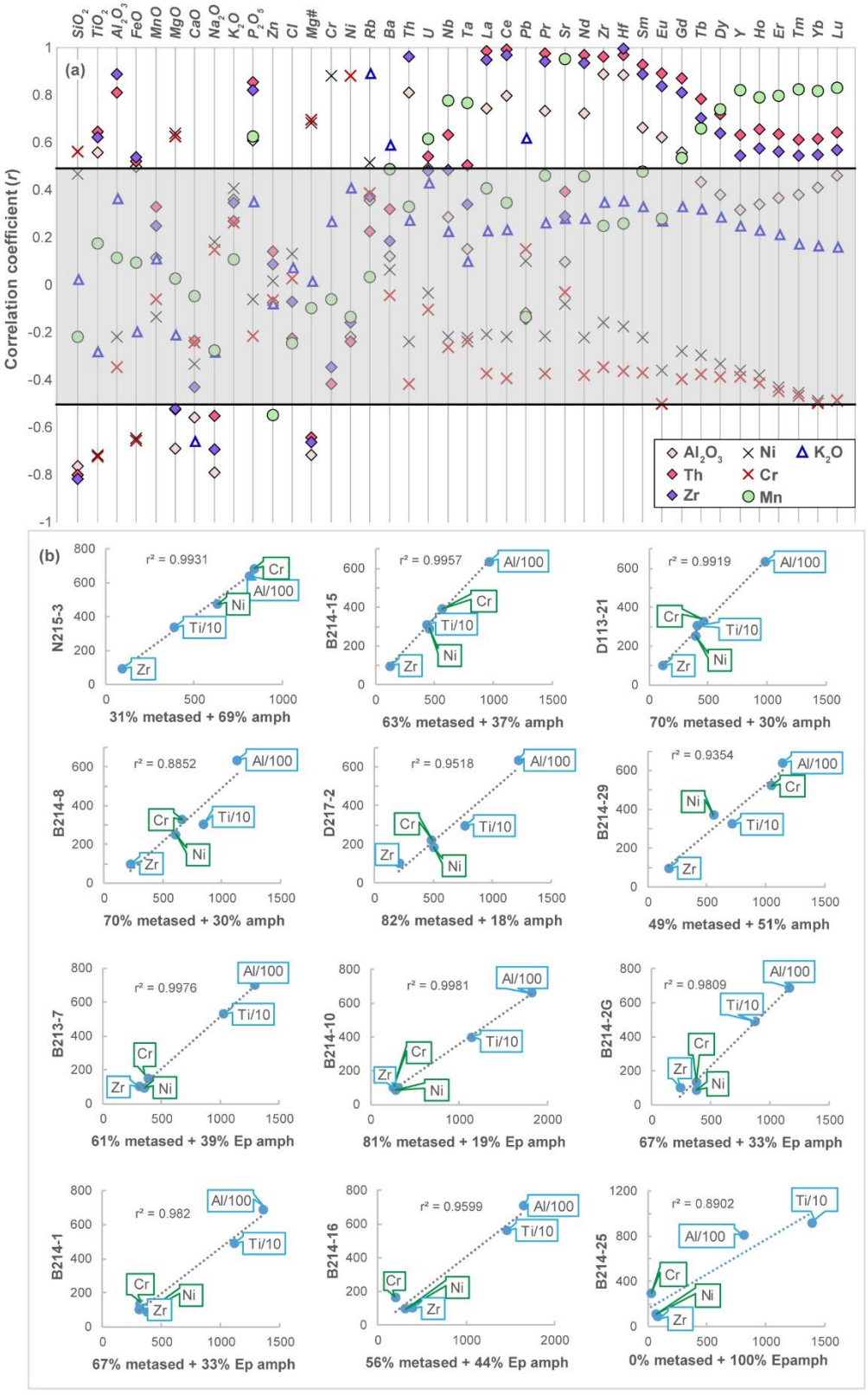
(a)
Correlation coefficient (r)
SiO2 TiO2 Al2O3 FeO MnO MgO CaO Na2O K2O P2O5 Zn Cl Mg# Cr Ni Rb Ba Th U Nb Ta La Ce Pb Pr Sr Nd Zr Hf Sm Eu Gd Tb Dy Y Ho Er Tm Yb Lu
Al2O3 Ni K2O
Th Cr
Zr Mn
(b)
N215-3
r² = 0.9931
31% metased + 69% amph
B214-15
r² = 0.9957
63% metased + 37% amph
D113-21
r² = 0.9919
70% metased + 30% amph
B214-8
r² = 0.8852
70% metased + 30% amph
D217-2
r² = 0.9518
82% metased + 18% amph
B214-29
r² = 0.9354
49% metased + 51% amph
B213-7
r² = 0.9976
61% metased + 39% Ep amph
B214-10
r² = 0.9981
81% metased + 19% Ep amph
B214-2G
r² = 0.9809
67% metased + 33% Ep amph
B214-1
r² = 0.982
67% metased + 33% Ep amph
B214-16
r² = 0.9599
56% metased + 44% Ep amph
B214-25
r² = 0.8902
0% metased + 100% Epamph
Al/100
Ti/10
Cr
Ni
Zr

1064

Fig. 10. a) coefficient of correlation showing the similarity in behavior of distinct groups of
1065 elements/components comprising the matrix samples. The values are given in Table 4. In particular, the strong correlation among Cr, Ni, and Mg suggest a metamafic end-member while the Al_2O_3, Th, and Zr contents of the matrix are strongly correlated with its LREE content indicating a metasedimentary end-member. The strong correlation of MnO with HREE content of the matrix meanwhile indicates strong control of certain minerals (e.g. garnet) in the chemistry of the matrix. Positive correlation between K_2O, Rb, and Ba on the other hand is related to the growth and abundance of Stage 3 replacement phases in the matrix samples. b) Fitting results between measured matrix composition (*y*-axis) and varying ratios of metasedimentary (N215-4) and metamafic (D113-9 and D113-5) blocks in the *x*-axis. The metased:metamafic ratio with the highest r^2 was used to determine the concentration of other elements resulting to the modelled matrix composition.

1066

1067

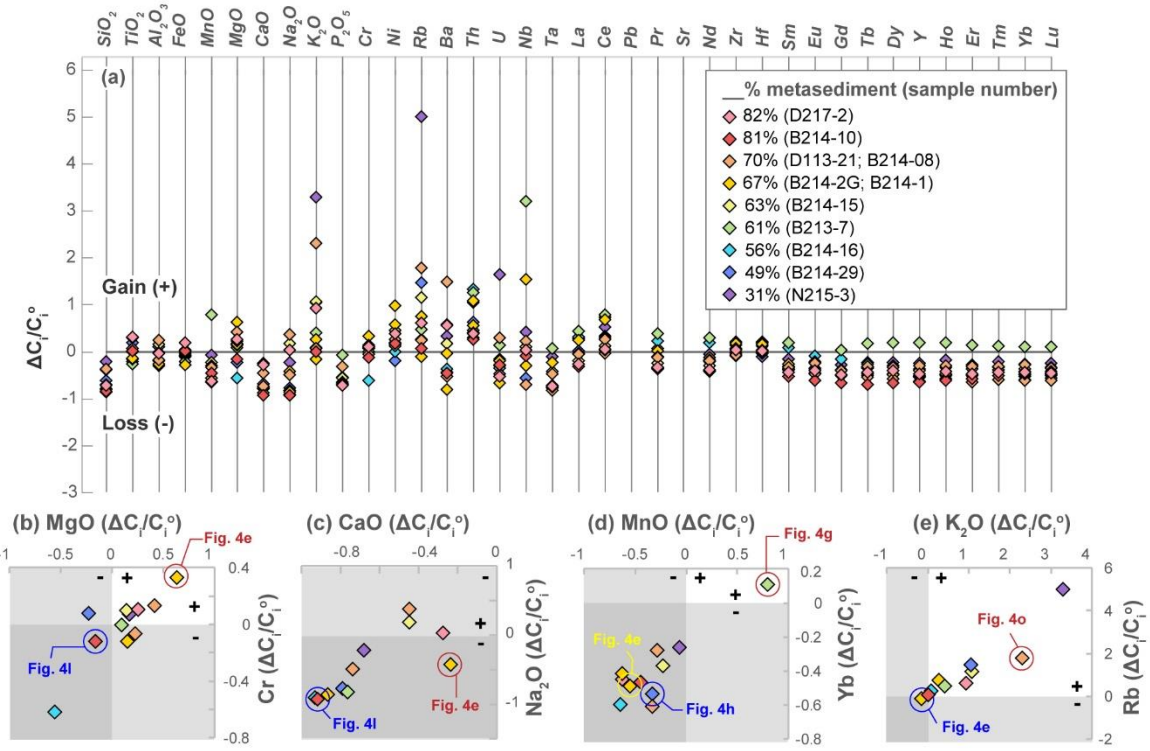

Fig. 11. a) Mass balance calculations showing the relative gains (+) and losses (-) in the matrix samples in terms of b) MgO and Cr, c) CaO and Na_2O, d) MnO and Yb, and e) K_2O and Rb. Also indicated are the representative photomicrographs of notable samples which exhibit systematic gains and losses apparently indicating the strong control of phase assemblage in the early leaching process, and later fluid infiltration.

1068

1069

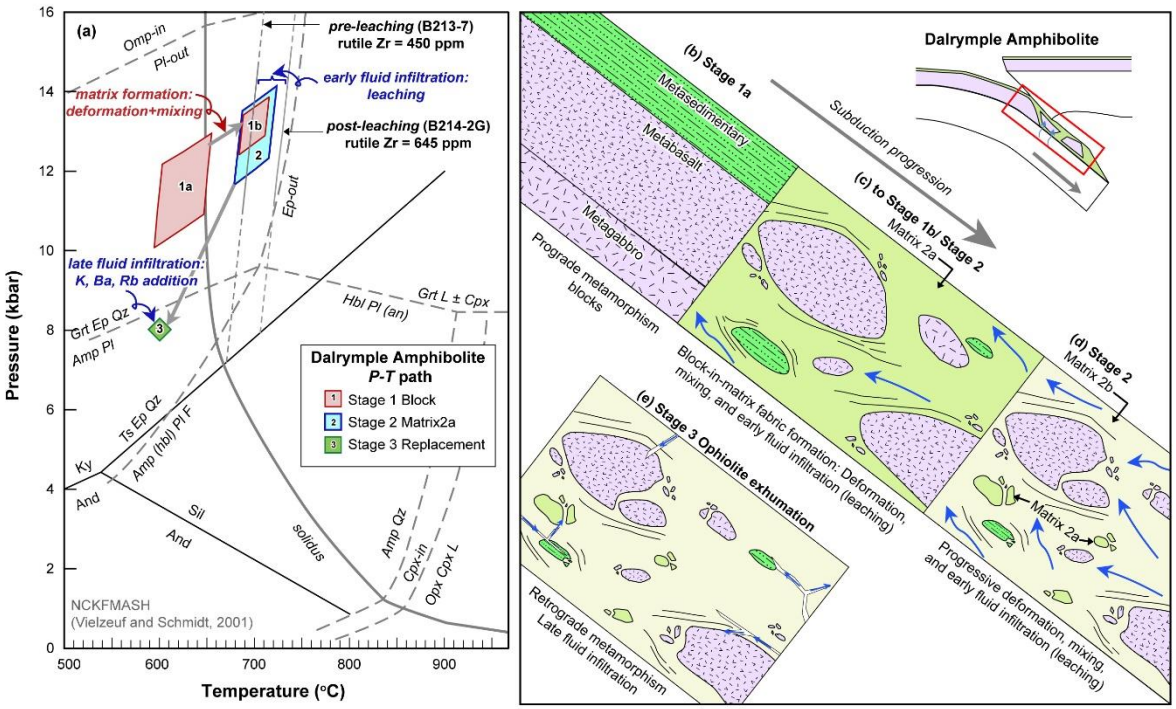

Fig. 12. a) Updated *P-T* history of the Dalrymple Amphibolite (modified from Valera et al., 2021) and its b–e) schematic representation. b,c) One evidence on the approximate timing of matrix formation as the sequence was subducted towards peak *P-T* conditions is the ten-fold increase in Nb content of rutile grains included in Stage 1b garnet relative to those in the garnet core (Stage 1a; Fig. 4p). The timing of early fluid infiltration (Fig. 12a, c, d) was constrained by the mean maximum Zr content of rutile (cf. Penniston-Dorland et al., 2018) in B213-7 and B214-2G. B213-7 did not reflect losses in garnet-related elements (i.e. MnO, HREEs; Fig. 11d) while B214-2G which exhibits notable losses in these elements recorded higher peak *P-T* conditions marking the maximum *P-T* conditions by which time leaching has already commenced (Fig. 12a, c, d). The peak *T* for B214-2G is slightly higher than those constrained for Stage 2 by Valera et al. (2021) albeit *P* cannot be constrained for this sample. This early fluid infiltration therefore likely started close to or at peak *P-T* conditions (Stage 2; Fig. 12c, d) possibly promoted by the extensive deformation of the sequence at this time. e) Finally, during ophiolite exhumation (Stage 3), later fluid infiltration resulted in the growth of replacement minerals (e.g. muscovite), and the addition of fluid mobile elements/components such as K_2O, Ba, and Rb in the matrix samples. Blue arrows in Figs. 12c–e represent infiltrating fluid.

1070

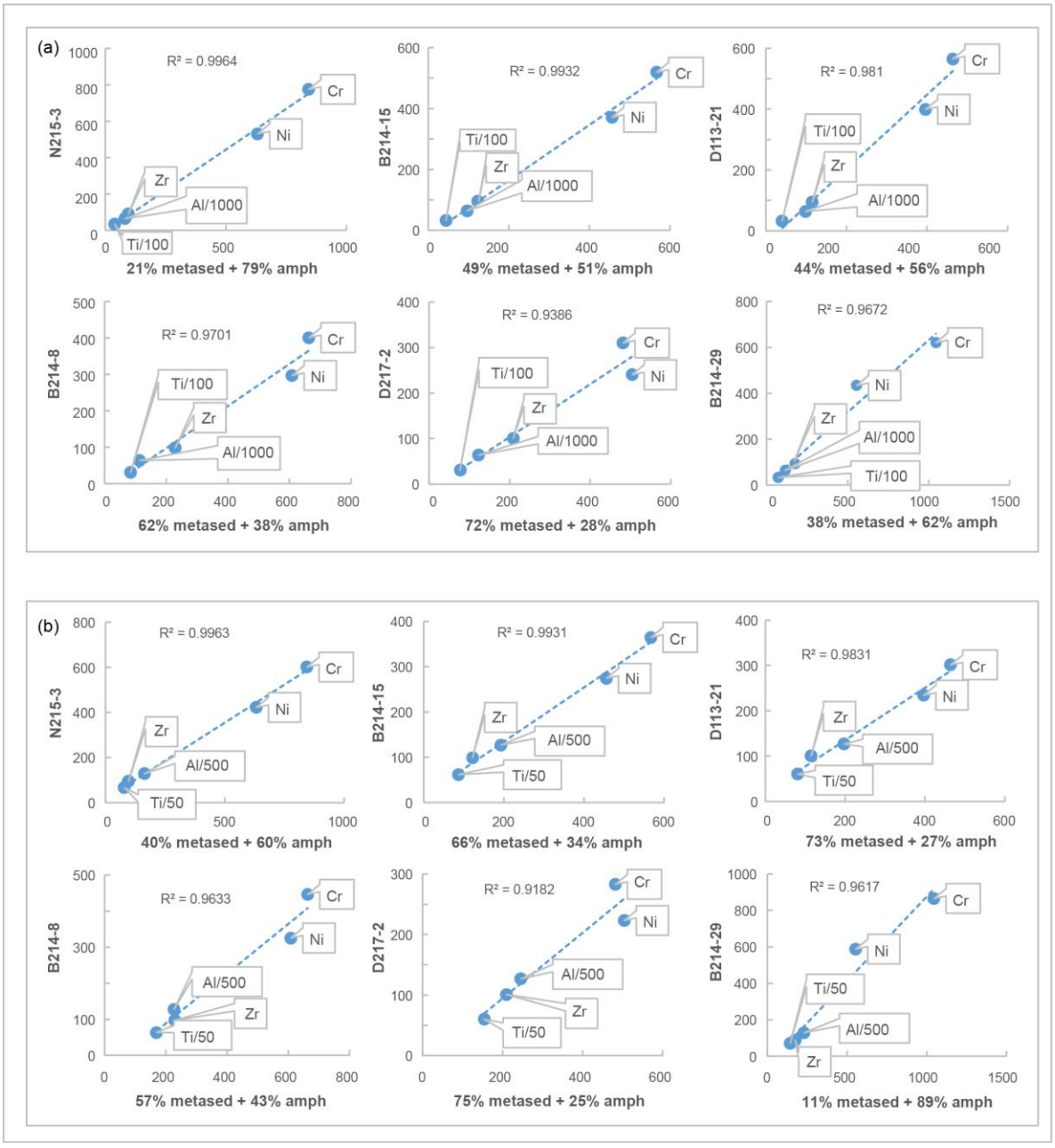

Fig. S1 showing fitting results between measured matrix composition (*y*-axis) and varying ratios of metasedimentary (N215-4) and amphibolite block (D113-9) in the *x*-axis. a) uses the highest denominator values i.e. Ti/100 Al/1000 while b) uses lower values Ti/50, Al/500 than in (a) but higher than in Fig. 10b.

Table 1. Summary of samples used in this study

Sample number	Locality			Field occurrence	Lithology	Major mineral assemblage [+secondary]	Accessory minerals	Whole-rock chemistry
	Area	Latitude	Longitude					
B213-4	Botoon	10°8'7.1"N	118°48'47.7"E	Block	Amphibolite	Camp + Pl [+Ab]	Ilm	○
B213-7	Botoon	10°8'7.1"N	118°48'47.7"E	Matrix2a	Ky-Grt schist	Ky + Grt + Ilm [+Ms +Chl]	Rt + Qz + Zrn + Ap	○
B213-8	Botoon	10°8'7.1"N	118°48'47.7"E	Block	Grt amphibolite	Camp + Grt + Qz + Ep [+Chl +Ep]	Rt + Ilm + Zrn + Ap	○
B213-9	Botoon	10°8'7.1"N	118°48'47.7"E	Block	Grt amphibolite	Camp + Grt + Qz + Ep + Ky [+Chl +Ep]	Rt + Ilm + Zrn + Ap	○
B214-1	Botoon	10°7'44.2"N	118°48'40.2"E	Matrix2a and 2b	Ky-Camp schist	Camp + Ky + Bt + Ilm [+Ms +Chl]	Ap + Tur	○
B214-2G	Botoon	10°7'44.2"N	118°48'40.2"E	Matrix2a	Ky-Grt-Bt-Camp schist	Camp + Grt + Ky + St + Bt [+Chl]	Rt + Ilm + Zrn + Ap + Chl	○
B214-2H	Botoon	10°7'44.2"N	118°48'40.2"E	Block	Amphibolite	Camp + Qz [+Chl]	Rt + Ilm + Zrn + Ep	○
B214-7E	Botoon	10°7'44.0"N	118°48'40.4"E	Block	Ep amphibolite	Camp + Ep + Qz	Rt + Zrn + Ilm + Ttn	○
B214-7C	Botoon	10°7'44.0"N	118°48'40.4"E	Block	Metacarbonate	Cb + Ep + Camp + Rt	Ilm + Ttn + Chl	○
B214-8	Botoon	10°7'44.4"N	118°48'40.6"E	Matrix2a and 2b	Ky-Camp-Bt schist	Matrix2a and 2b: Camp + Oam + Ky + Ilm + Bt [+Ms +Chl]	Grt + Ap	○
B214-10	Botoon	10°7'44.7"N	118°48'41"E	Matrix2a	Ky-Camp-Bt schist	Ky + Ilm + Bt [+Ms +Chl]	Mag + Ap + Tur + Oam + Camp + Grt	○
B214-13	Botoon	10°7'44.7"N	118°48'41"E	Block	Amphibolite	Ky + Grt + Ilm [+Ms +Chl]	Rt + Qz + Zrn + Ap	○
B214-14	Botoon	10°7'45.8"N	118°48'41"E	Matrix2a	Ky-Ep-Grt schist	Ky + Grt + Ep + Ilm + Bt [+Ms +Ep +Chl]	Rt + Ap + Zrn + Chl	
B214-15	Botoon	10°7'45.8"N	118°48'40.4"E	Matrix 2a	Ky-Camp schist	Camp + Grt + Qz + Ky [+Ms +Chl]	Ilm + Bt + Ap	○
B214-16	Botoon	10°7'45.8"N	118°48'40.4"E	Matrix 2a	Ky schist	Ky + Ilm + Qz [+Ms +Chl]	Ap	○
B214-21	Botoon	10°7'45.0"N	118°48'40.1"E	Block	Grt amphibolite	Camp + Grt + Ep + Qz [+Act +Ep +Chl]	Ky + Bt + Ap + Rt + Ilm + Zrn	○

1071

Table 1. continued

Sample number	Locality			Field occurrence	Lithology	Major mineral assemblage [+secondary]	Accessory minerals	Whole-rock chemistry
	Area	Latitude	Longitude					
N215-11	Nanad	10°7'23.8"N	118°48'25.8"E	Block	Ep amphibolite	Camp + Ep + Qz	Ky + Pl + Ap	○
D113-5	Dalrymple	10°6'39.4"N	118°48'41.1"E	Block	Ep amphibolite	Camp + Ep + Pl + Qz [+Act +Ab]	Rt + Zrn + Ttn + Ap + Bt	○
D113-9	Dalrymple	10°6'41.6"N	118°48'36.7"E	Block	Amphibolite	Camp + Ep + Pl + Qz [+Act +Chl +Ab]	Rt + Zrn + Ttn	○
D113-10	Dalrymple	10°6'41.6"N	118°48'36.7"E	Block	Ep amphibolite	Camp + Ep + Pl + Qz [+Chl +Ab]	Rt + Zrn + Ttn + Ap + Bt	○
D113-11	Dalrymple	10°6'41.6"N	118°48'36.7"E	Block	Amphibolite	Camp + Ep + Pl + Qz [+Act +Ab]	Rt + Zrn	○
D113-13	Dalrymple	10°6'41.6"N	118°48'36.7"E	Block	Ep amphibolite	Camp + Ep + Pl + Qz [+Chl +Ab]	Rt + Zrn + Ttn + Ap	○
D113-14A	Dalrymple	10°6'42.5"N	118°48'36.1"E	Block	Amphibolite	Camp + Pl + Qz + Ep [+Act +Chl +Ep]	Rt + Zrn + Ap + Ms	○
D113-14G	Dalrymple	10°6'42.5"N	118°48'36.1"E	Block	Grt amphibolite	Camp + Grt + Pl + Qz + Ep [+Act +Chl +Ep]	Rt + Zrn + Ap + Ms	○
D113-15	Dalrymple	10°6'42.5"N	118°48'36.1"E	Block	Grt amphibolite	Camp + Grt + Pl + Qz + Ep [+Chl +Ep +Ab]	Rt + Ap + Ms + Ccp + Py	○
D113-16	Dalrymple	10°6'43.3"N	118°48'36.3"E	Block	Ep amphibolite	Camp + Ep + Pl + Qz [+Chl +Ab]	Rt + Zrn + Ttn + Ap	○
D113-18	Dalrymple	10°6'43.3"N	118°48'36.3"E	Block	Grt amphibolite	Camp + Grt + Pl + Qz + Ep + Bt [+Act +Chl +Ep +Ab]	Rt + Zrn + Ap	○
D113-21	Dalrymple	10°6'42.5"N	118°48'36.1"E	Block	Ky-Camp schist	Camp + Qz + Bt + Ky(?) [+Ms +Chl]	Ap + Ilm	○
D215-7	Dalrymple	10°6'43.3"N	118°48'36.3"E	Block	Ep-Bt-Ms schist	Bt + Ms + Pl + Ep +Qz [+Chl]	Rt + Ilm + Zrn + Ap	○
D217-2	Dalrymple	10°6'43.3"N	118°48'36.3"E	Block	Ky-Camp-Bt schist	Bt + Camp + Ky + Ilm + Qz [+Ms +Chl]	Ap	○

1072

Table 2 Major and trace element data of blocks in Dalrymple Amphibolite

Lithology	Ep amphibolite						
Locality	Dalrymple				Botoon		Nanad
Sample	D113-5	D113-10	D113-13	D113-16	B214-7E	B214-22	N215-11
in wt.%							
SiO_2	48.24	47.28	43.90	41.99	46.74	45.61	46.20
TiO_2	1.52	0.91	0.81	0.90	0.70	1.92	0.14
Al_2O_3	15.15	14.92	17.55	19.17	11.95	14.32	18.69
Fe_2O_3*	11.44	9.32	9.89	11.20	10.28	13.88	5.13
MnO	0.19	0.24	0.21	0.14	0.60	0.65	0.11
MgO	6.32	8.54	6.77	7.54	14.23	7.93	9.69
CaO	11.98	15.15	17.28	15.62	12.16	12.72	16.38
Na_2O	3.32	0.98	1.27	1.21	1.12	0.79	1.25
K_2O	0.62	0.38	0.32	0.43	0.26	0.21	0.27
P_2O_5	0.16	0.49	0.35	0.02	0.01	0.08	0.06
SrO	0.03	0.05	0.07	0.07	0.02	0.04	0.03
BaO	0.02	0.02	0.01	0.01	0.02	0.02	0.02
Cr_2O_3	0.04	0.06	0.04	0.01	0.12	0.02	0.14
Ni	0.01	0.02	0.02	0.01	0.07	0.01	0.02
Zn	0.01	0.01	0.01	0.01	0.02	0.01	0.01
Total	100.13	100.08	100.15	100.03	99.85	99.75	100.26
LOI	1.08	1.72	1.65	1.71	1.54	1.55	2.14
in ppm							
Rb	10.20	9.20	5.75	10.80	2.80	3.50	6.20
Th	0.21	1.17	0.69	0.04	8.21	0.31	0.61
U	0.15	2.16	6.85	0.06	1.22	3.13	3.13
Nb	2.73	3.68	2.99	0.57	10.80	6.74	0.25
Ta	0.42	0.75	0.59	0.29	0.98	0.86	0.36
La	4.32	4.07	2.24	0.86	23.10	5.27	0.64
Ce	10.50	9.36	4.96	2.32	51.80	13.90	1.30
Pb	2.00	6.00	8.00	3.00	12.00	17.00	10.00
Pr	2.04	1.41	0.86	0.39	5.70	2.48	0.21
Nd	10.40	6.88	4.32	2.51	22.40	13.60	1.00
Zr	90.50	39.00	30.50	15.00	95.00	112.00	6.00
Hf	2.61	1.34	1.16	0.54	2.60	3.27	0.21
Sm	3.39	1.99	1.46	0.98	4.64	4.65	0.47
Eu	1.28	0.73	0.58	0.60	1.03	1.76	0.27
Gd	4.88	2.57	2.32	1.32	4.38	6.12	0.73
Tb	0.86	0.49	0.46	0.25	0.69	1.17	0.15
Dy	5.77	3.17	3.58	1.67	4.20	7.57	1.09
Y	32.30	20.60	25.30	10.10	23.30	41.90	6.24
Ho	1.27	0.74	0.85	0.40	0.88	1.68	0.22
Er	3.62	2.36	2.78	1.17	2.49	4.75	0.60
Tm	0.54	0.40	0.42	0.18	0.42	0.67	0.10
Yb	3.63	2.64	2.84	1.16	2.52	4.24	0.60
Lu	0.47	0.38	0.43	0.17	0.38	0.59	0.08

L.O.I.=loss on ignition; b.d.=below detection limit; n.d.=not determined; Fe_2O_3* = total Fe

1073

Table 2 Continued

Lithology	Amphibolite					
Locality	Dalrymple			Botoon		
Sample	D113-9	D113-11	D113-14A	B213-4	B214-2H	B214-13
in wt.%						
SiO_2	47.06	48.12	45.02	46.69	45.58	44.97
TiO_2	0.60	0.31	1.59	0.57	0.81	0.88
Al_2O_3	12.05	10.84	13.93	13.47	13.94	14.24
Fe_2O_3*	11.02	10.41	12.79	10.40	11.58	11.93
MnO	0.38	0.32	0.35	0.39	0.38	0.56
MgO	14.30	15.12	12.72	14.14	14.26	13.13
CaO	10.36	10.90	9.46	9.24	9.23	9.63
Na_2O	2.05	1.91	2.04	2.36	1.72	1.58
K_2O	0.38	0.42	0.51	0.45	0.48	0.59
P_2O_5	0.01	0.12	0.15	0.04	0.03	0.04
SrO	0.01	0.01	0.01	0.01	0.01	0.01
BaO	0.02	0.02	0.01	0.01	0.02	0.02
Cr_2O_3	0.14	0.04	0.09	0.03	0.13	0.06
Ni	0.06	0.02	0.04	0.01	0.06	0.02
Zn	0.02	0.02	0.01	0.02	0.02	0.02
Total	99.99	99.92	100.07	99.67	100.11	99.71
LOI	1.53	1.35	1.35	1.85	1.86	2.03
in ppm						
Rb	8.65	7.70	12.20	11.50	12.30	16.20
Th	1.10	0.70	2.25	0.03	1.48	23.60
U	0.12	0.07	0.34	0.12	0.26	1.71
Nb	4.28	0.50	30.70	1.63	12.50	7.99
Ta	0.41	0.23	2.24	0.23	1.24	0.88
La	4.26	5.92	8.32	0.62	5.39	66.80
Ce	12.50	13.60	22.30	2.14	16.80	149.00
Pb	b.d.	b.d.	2.00	8.00	2.00	6.00
Pr	2.06	1.90	3.30	0.50	2.54	16.40
Nd	10.70	8.66	16.50	2.89	14.40	60.90
Zr	86.00	8.50	164.00	38.50	130.00	60.00
Hf	2.54	0.43	4.24	1.26	3.67	2.09
Sm	3.40	2.29	5.39	1.25	4.89	12.80
Eu	0.97	0.80	1.44	1.53	1.44	2.97
Gd	4.01	2.29	6.56	2.11	5.81	12.90
Tb	0.66	0.35	1.14	0.46	1.02	2.24
Dy	4.35	1.89	7.15	3.41	6.52	14.10
Y	25.30	10.30	41.40	18.40	37.10	73.50
Ho	0.91	0.38	1.55	0.75	1.37	2.84
Er	2.67	0.96	4.63	2.19	4.11	7.77
Tm	0.39	0.15	0.67	0.32	0.62	1.09
Yb	2.62	0.98	4.24	1.92	3.93	6.54
Lu	0.38	0.15	0.61	0.27	0.60	0.85

L.O.I.=loss on ignition; b.d.=below detection limit; n.d.=not determined; Fe_2O_3* = total Fe

1074

Table 2. Continued

Lithology	Grt amphibolite						
Locality	Dalrymple			Botoon			
Sample	D113-14G	D113-15	D113-18	B213-8	B213-9		B214-21
in wt.%							
SiO_2	39.76	53.63	47.46	44.34	38.03	41.83	43.16
TiO_2	2.52	2.90	1.08	1.36	1.73	1.42	2.20
Al_2O_3	17.27	15.83	14.66	14.75	19.52	21.55	14.02
Fe_2O_3*	21.30	14.01	15.90	16.55	22.63	11.15	15.84
MnO	0.34	0.26	0.45	1.22	3.03	0.32	0.57
MgO	6.99	3.17	8.69	10.86	9.39	11.63	11.02
CaO	8.86	4.55	6.91	7.50	4.38	6.98	8.90
Na_2O	1.25	4.72	0.97	1.21	0.42	1.38	1.33
K_2O	1.09	0.54	0.81	0.36	0.20	1.50	0.51
P_2O_5	0.01	0.03	0.13	0.03	0.03	0.16	0.06
SrO	0.02	0.03	0.01	0.01	0.01	0.01	0.01
BaO	b.d.	0.03	0.02	0.02	0.01	0.04	0.01
Cr_2O_3	0.02	b.d.	0.00	0.01	0.01	0.05	0.02
Ni	0.02	0.00	0.00	0.01	0.01	0.04	0.01
Zn	0.01	0.01	0.07	0.08	0.03	0.01	0.02
Total	100.27	100.07	99.80	99.33	99.41	100.06	99.32
LOI	39.76	53.63	47.46	1.03			1.63
in ppm							
Rb	29.50	8.05	27.30	8.85	6.70		10.40
Th	0.05	0.06	1.00	0.20	3.26		1.10
U	0.03	0.08	0.13	0.22	0.44		1.00
Nb	0.77	0.91	1.45	1.44	20.80		20.30
Ta	0.66	0.69	0.50	0.75	2.77		1.95
La	0.90	1.01	4.64	2.59	9.92		4.63
Ce	2.82	2.80	11.10	7.66	20.30		12.80
Pb	b.d.	2.00	2.00	b.d.	b.d.		4.00
Pr	0.51	0.47	1.63	1.44	2.26		2.06
Nd	2.79	2.40	8.66	8.10	8.08		10.60
Zr	16.50	27.00	51.00	60.00	90.50		121.00
Hf	0.56	0.82	1.56	1.99	2.76		3.61
Sm	0.98	0.90	2.68	3.09	1.80		3.87
Eu	0.73	0.70	0.99	1.04	0.49		1.14
Gd	1.68	1.40	3.67	4.06	3.11		5.44
Tb	0.35	0.27	0.68	0.78	0.89		1.11
Dy	2.50	1.87	4.84	5.46	8.14		7.50
Y	15.40	11.00	27.90	31.90	58.80		41.30
Ho	0.62	0.41	1.07	1.23	2.20		1.62
Er	1.80	1.16	3.42	3.69	7.56		4.74
Tm	0.30	0.18	0.48	0.57	1.24		0.72
Yb	1.85	1.26	3.22	3.89	8.83		4.75
Lu	0.29	0.17	0.48	0.54	1.37		0.67

L.O.I.=loss on ignition; b.d.=below detection limit; n.d.=not determined; Fe_2O_3* = total Fe

1075

Table 2 Continued

Lithology	Ky-Ilm-Grt quartzite	Ep-Bt-Ms schist	Camp-Ky-quartzite	Metacarbonate
Locality	Nanad	Dalrymple	Botoon	Botoon
Sample	N215-4	D215-7	B214-26	B214-7C
in wt.%				
SiO_2	76.34	42.99	57.96	28.41
TiO_2	0.46	3.26	1.20	0.59
Al_2O_3	11.76	19.22	18.58	13.89
Fe_2O_3*	5.46	15.64	11.18	9.32
MnO	0.42	0.14	0.20	0.91
MgO	2.01	3.36	4.62	5.20
CaO	0.70	3.84	2.32	27.32
Na_2O	0.10	3.19	0.47	0.34
K_2O	0.99	4.77	1.62	0.06
P_2O_5	0.34	1.31	0.11	0.06
SrO	b.d.	0.03	0.01	0.06
BaO	0.02	0.13	0.03	0.01
Cr_2O_3	0.01	0.04	0.01	0.06
Ni	0.01	0.01	0.01	0.02
Zn	0.00	0.01	0.01	0.01
Total	99.72	100.04	99.72	99.74
LOI	1.1	2.09	1.4	13.49
in ppm				
Rb	37.80	106.00	77.00	0.55
Th	9.77	8.62	0.92	10.90
U	0.70	0.93	0.29	3.19
Nb	5.01	90.00	2.91	10.40
Ta	1.55	5.14	1.09	1.17
La	44.20	75.70	4.39	55.90
Ce	70.80	118.00	10.50	74.50
Pb	2.00	4.00	b.d.	33.00
Pr	11.00	15.40	1.54	14.50
Nd	43.30	58.90	7.28	59.80
Zr	106.00	275.00	68.50	120.00
Hf	3.00	6.57	2.14	3.29
Sm	8.40	11.30	2.21	12.60
Eu	1.69	3.33	0.79	2.83
Gd	7.72	10.20	3.24	12.00
Tb	1.06	1.49	0.64	1.79
Dy	6.47	8.54	4.54	11.10
Y	37.60	47.60	26.90	70.00
Ho	1.35	1.71	1.09	2.44
Er	4.22	4.51	3.24	7.10
Tm	0.60	0.63	0.51	1.04
Yb	4.07	3.64	3.52	6.44
Lu	0.60	0.49	0.48	0.98

L.O.I.=loss on ignition; b.d.=below detection limit; n.d.=not determined; Fe_2O_3* = total Fe

1076

Table 3. Measured major and trace element data of matrix in Dalrymple Amphibolite

Lithology	Ky-Grt-Bt-Camp schist	Ky-Camp schist	Ky-Camp-Bt schist	Ky-Camp schist	Ky schist	Ky-Grt-Camp schist
Locality	Botoon	Dalrymple	Dalymple	Botoon	Botoon	Botoon
Sample	B214-2G	D113-21	D217-2	B214-15	B214-16	B214-25
in wt.%						
SiO_2	41.83	51.78	38.67	51.87	28.75	38.14
TiO_2	1.42	0.65	1.22	0.70	2.34	2.29
Al_2O_3	21.55	17.84	22.01	17.56	29.99	15.25
Fe_2O_3*	11.15	8.57	14.85	9.27	23.93	23.89
MnO	0.32	0.35	0.29	0.40	0.36	0.52
MgO	11.63	9.80	10.17	9.63	5.52	10.27
CaO	6.98	2.40	3.38	3.03	1.20	6.36
Na_2O	1.38	1.14	0.89	1.25	0.46	0.99
K_2O	1.50	3.21	3.25	2.02	2.87	0.61
P_2O_5	0.16	0.09	0.16	0.12	0.58	0.04
SrO	0.01	0.01	0.01	0.01	0.01	0.01
BaO	0.04	0.06	0.06	0.03	0.04	0.01
Cr_2O_3	0.05	0.07	0.07	0.08	0.03	0.00
Ni	0.04	0.04	0.05	0.04	0.03	0.01
Zn	0.01	0.01	0.01	0.01	0.02	0.01
Total	100.06	100.26	99.80	99.50	100.10	99.79
LOI	1.98	4.25	4.72	3.47	3.98	1.38
in ppm						
Rb	54.10	101.00	104.00	76.60	106.00	22.10
Th	28.80	11.60	22.60	12.60	42.60	11.10
U	0.88	0.85	0.56	0.54	0.97	0.31
Nb	22.60	7.34	10.10	6.93	16.10	4.88
Ta	1.91	0.80	0.70	0.85	0.98	0.68
La	80.80	27.40	54.00	31.40	115.00	30.10
Ce	180.00	64.20	127.00	72.10	252.00	66.40
Pb	2.00	15.00	5.00	7.00	10.00	3.00
Pr	17.20	6.59	12.50	7.58	28.70	7.33
Nd	59.50	25.20	46.00	28.80	113.00	28.20
Zr	239.00	115.00	209.00	122.00	397.00	83.50
Hf	6.73	3.48	5.92	3.63	11.20	2.54
Sm	9.34	5.30	8.43	5.85	22.20	5.42
Eu	1.96	1.40	1.85	1.20	4.52	1.65
Gd	7.00	4.95	7.17	4.96	18.10	5.82
Tb	1.04	0.80	1.09	0.81	2.38	1.01
Dy	6.66	4.91	7.17	5.21	12.10	7.13
Y	36.60	29.90	37.10	27.40	53.50	41.90
Ho	1.47	1.07	1.46	1.05	2.12	1.68
Er	4.29	3.23	4.19	3.00	5.61	5.05
Tm	0.60	0.46	0.62	0.46	0.78	0.79
Yb	4.20	3.27	4.20	2.95	5.17	5.37
Lu	0.59	0.43	0.60	0.45	0.78	0.75

L.O.I.=loss on ignition; b.d.=below detection limit; n.d.=not determined; Fe_2O_3* = total Fe

Table 3. Continued

Lithology	Ky-Grt schist	Ky-Camp-Bt schist	Ky-Camp schist	Ky-Camp-Bt schist	Ky-Hbl-Qz schist	Grt-Hbl-Bt schist
Locality	Botoon	Botoon	Botoon	Botoon	Botoon	Nanad
Sample	B213-7	B214-10	B214-01	B214-08	B214-29	N215-3
in wt.%						
SiO_2	36.16	32.65	34.23	39.40	49.92	49.92
TiO_2	1.65	1.86	1.78	1.37	0.63	0.63
Al_2O_3	23.56	33.64	24.54	20.78	14.90	14.90
Fe_2O_3*	15.83	18.66	19.69	15.19	9.53	9.53
MnO	1.50	0.57	0.33	0.57	0.41	0.41
MgO	10.25	6.61	10.13	14.74	13.85	13.85
CaO	3.05	0.63	1.48	1.97	2.63	2.63
Na_2O	0.60	0.14	0.41	0.73	1.26	1.26
K_2O	3.03	2.55	2.81	1.83	2.74	2.74
P_2O_5	0.63	0.27	0.26	0.35	0.12	0.12
SrO	0.02	0.01	0.01	0.01	0.01	0.01
BaO	0.08	0.03	0.01	0.02	0.03	0.03
Cr_2O_3	0.06	0.04	0.04	0.09	0.12	0.12
Ni	0.03	0.03	0.04	0.06	0.06	0.06
Zn	0.01	0.01	0.01	0.01	0.01	0.01
Total	100.14	100.08	100.06	100.13	99.68	99.68
LOI	3.68	2.39	4.29	3	4.39	3.46
in ppm						
Rb	104.00	98.30	133.00	77.90	105.00	122.00
Th	35.80	28.30	27.30	21.70	16.10	8.95
U	1.45	1.21	0.46	0.60	0.53	0.91
Nb	45.30	11.70	7.96	3.14	3.86	7.35
Ta	3.11	0.94	0.58	0.46	0.43	0.79
La	107.00	70.70	79.20	66.00	45.40	24.30
Ce	220.00	172.00	175.00	144.00	101.00	53.80
Pb	6.00	3.00	b.d.	2.00	b.d.	8.00
Pr	27.20	16.80	18.90	15.80	10.70	5.95
Nd	103.00	60.80	71.20	58.30	39.20	22.60
Zr	310.00	307.00	311.00	229.00	175.00	96.00
Hf	8.87	8.54	8.75	6.31	4.92	2.75
Sm	20.00	9.86	13.00	9.96	6.97	4.78
Eu	3.19	1.78	2.61	1.66	1.32	1.07
Gd	17.90	6.81	11.10	7.19	5.48	4.30
Tb	3.03	0.88	1.70	0.93	0.84	0.70
Dy	19.40	6.06	11.00	5.36	5.34	4.42
Y	110.00	37.10	56.60	27.60	27.30	25.00
Ho	4.10	1.48	2.32	1.09	1.08	1.00
Er	11.80	4.97	6.78	2.87	3.12	2.61
Tm	1.69	0.82	0.94	0.47	0.45	0.41
Yb	11.30	6.01	6.07	3.08	2.91	2.62
Lu	1.59	0.93	0.78	0.45	0.44	0.39

L.O.I.=loss on ignition; b.d,=below detection limit; n.d.=not determined; Fe_2O_3*=total Fe

1077

Table 4. Correlation matrices for the measured matrix composition in Table 3

	SiO_2	TiO_2	Al_2O_3	FeO*	MnO	MgO	CaO	Na_2O	K_2O	P_2O_5	Cr	Ni	Rb	Ba	Th	U	Nb	Ta	La	Ce	Pb	Pr	Sr	Nd	Zr	Hf	Sm	Eu	Gd	Tb	Dy	Y	Ho	Er	Tm	Yb	Lu
SiO_2	1.00																																			
TiO_2	0.86	1.00																																		
Al_2O_3	0.58	0.31	1.00																																	
FeO*	0.78	0.92	0.25	1.00																																
MnO	0.05	0.03	0.01	0.01	1.00																															
MgO	0.25	0.29	0.47	0.27	0.00	1.00																														
CaO	0.04	0.00	0.31	0.01	0.00	0.07	1.00																													
Na_2O	0.56	0.36	0.62	0.42	0.07	0.21	0.45	1.00																												
K_2O	0.00	0.08	0.13	0.04	0.01	0.04	0.43	0.08	1.00																											
P_2O_5	0.39	0.24	0.38	0.18	0.39	0.10	0.16	0.28	0.12	1.00																										
Cr	0.32	0.52	0.12	0.42	0.00	0.40	0.06	0.02	0.07	0.05	1.00																									
Ni	0.22	0.51	0.05	0.41	0.02	0.41	0.11	0.03	0.17	0.00	0.78	1.00																								
Rb	0.00	0.06	0.13	0.02	0.00	0.00	0.59	0.15	0.79	0.10	0.15	0.27	1.00																							
Ba	0.01	0.04	0.01	0.09	0.24	0.03	0.00	0.02	0.35	0.17	0.00	0.00	0.05	1.00																						
Th	0.64	0.42	0.66	0.28	0.11	0.27	0.05	0.30	0.07	0.73	0.17	0.06	0.05	0.10	1.00																					
U	0.05	0.00	0.24	0.01	0.38	0.09	0.07	0.05	0.18	0.41	0.01	0.00	0.09	0.43	0.29	1.00																				
Nb	0.09	0.06	0.08	0.00	0.61	0.04	0.03	0.01	0.05	0.47	0.07	0.05	0.01	0.50	0.40	0.58	1.00																			
Ta	0.03	0.02	0.02	0.00	0.59	0.01	0.08	0.00	0.01	0.32	0.06	0.05	0.00	0.46	0.26	0.54	0.96	1.00																		
La	0.61	0.41	0.55	0.26	0.17	0.17	0.04	0.29	0.05	0.79	0.14	0.04	0.05	0.09	0.97	0.28	0.45	0.31	1.00																	
Ce	0.65	0.43	0.64	0.27	0.12	0.21	0.05	0.32	0.05	0.74	0.15	0.05	0.05	0.07	0.99	0.28	0.39	0.26	0.99	1.00																
Pb	0.18	0.14	0.01	0.08	0.02	0.06	0.14	0.03	0.38	0.00	0.02	0.01	0.27	0.18	0.02	0.03	0.00	0.01	0.03	0.04	1.00															
Pr	0.61	0.42	0.54	0.29	0.21	0.19	0.07	0.32	0.07	0.86	0.14	0.05	0.06	0.10	0.96	0.31	0.46	0.31	0.99	0.97	0.02	1.00														
Sr	0.03	0.01	0.01	0.00	0.91	0.00	0.00	0.04	0.08	0.42	0.00	0.01	0.03	0.43	0.16	0.41	0.79	0.75	0.22	0.16	0.00	0.26	1.00													
Nd	0.60	0.43	0.53	0.31	0.21	0.21	0.08	0.32	0.08	0.88	0.14	0.05	0.07	0.10	0.94	0.29	0.44	0.28	0.97	0.94	0.01	0.99	0.26	1.00												
Zr	0.67	0.39	0.79	0.29	0.06	0.27	0.18	0.48	0.12	0.68	0.12	0.02	0.14	0.03	0.93	0.24	0.24	0.12	0.90	0.94	0.02	0.89	0.08	0.88	1.00											
Hf	0.66	0.40	0.79	0.30	0.07	0.29	0.18	0.47	0.13	0.69	0.13	0.03	0.14	0.04	0.94	0.24	0.26	0.13	0.91	0.95	0.01	0.90	0.09	0.89	1.00	1.00										
Sm	0.52	0.39	0.44	0.31	0.23	0.22	0.09	0.28	0.11	0.91	0.13	0.05	0.09	0.13	0.87	0.29	0.44	0.28	0.90	0.86	0.00	0.95	0.30	0.98	0.79	0.81	1.00									
Eu	0.55	0.50	0.39	0.43	0.08	0.33	0.05	0.21	0.07	0.71	0.25	0.13	0.05	0.08	0.80	0.16	0.30	0.16	0.79	0.76	0.02	0.83	0.14	0.87	0.70	0.73	0.92	1.00								
Gd	0.46	0.38	0.31	0.31	0.29	0.21	0.06	0.23	0.11	0.86	0.16	0.08	0.08	0.16	0.76	0.26	0.50	0.33	0.80	0.74	0.01	0.87	0.39	0.91	0.66	0.68	0.97	0.91	1.00							
Tb	0.34	0.29	0.19	0.23	0.44	0.14	0.02	0.16	0.10	0.78	0.14	0.09	0.06	0.22	0.62	0.27	0.63	0.47	0.68	0.61	0.01	0.75	0.59	0.79	0.50	0.53	0.86	0.76	0.95	1.00						
Dy	0.31	0.26	0.15	0.20	0.55	0.10	0.01	0.15	0.08	0.67	0.15	0.11	0.05	0.23	0.52	0.27	0.70	0.55	0.59	0.52	0.00	0.66	0.71	0.67	0.41	0.44	0.73	0.61	0.84	0.96	1.00					
Y	0.24	0.21	0.10	0.14	0.68	0.07	0.00	0.12	0.06	0.57	0.15	0.13	0.03	0.27	0.40	0.31	0.76	0.64	0.48	0.41	0.00	0.53	0.82	0.54	0.30	0.32	0.58	0.44	0.69	0.86	0.96	1.00				
Ho	0.28	0.25	0.12	0.17	0.63	0.08	0.00	0.14	0.05	0.57	0.17	0.14	0.03	0.22	0.43	0.28	0.73	0.61	0.51	0.44	0.00	0.56	0.77	0.57	0.33	0.36	0.60	0.47	0.71	0.87	0.97	0.99	1.00			
Er	0.29	0.26	0.14	0.18	0.64	0.10	0.00	0.16	0.05	0.50	0.20	0.18	0.02	0.21	0.41	0.29	0.72	0.61	0.47	0.41	0.01	0.52	0.76	0.52	0.32	0.34	0.54	0.41	0.64	0.80	0.93	0.98	0.99	1.00		
Tm	0.31	0.28	0.15	0.19	0.68	0.10	0.00	0.18	0.03	0.49	0.22	0.21	0.01	0.19	0.38	0.31	0.70	0.59	0.43	0.38	0.02	0.48	0.76	0.48	0.30	0.32	0.50	0.36	0.59	0.75	0.88	0.96	0.96	0.99	1.00	
Yb	0.32	0.29	0.17	0.19	0.67	0.12	0.00	0.19	0.03	0.47	0.25	0.23	0.01	0.21	0.38	0.34	0.70	0.60	0.43	0.39	0.02	0.48	0.74	0.47	0.30	0.32	0.48	0.35	0.56	0.71	0.84	0.93	0.93	0.97	0.99	1.00
Lu	0.35	0.30	0.22	0.20	0.69	0.15	0.00	0.22	0.03	0.50	0.24	0.23	0.01	0.21	0.41	0.40	0.71	0.61	0.45	0.41	0.03	0.50	0.73	0.49	0.33	0.34	0.50	0.35	0.56	0.69	0.81	0.89	0.89	0.93	0.97	0.99	1.00

Table 5. Calculated major and trace element data of matrix in Dalrymple Amphibolite

Metamafic2a: Amphibolite (D113-9)						
_%metased1	31	67	70	49	70	82
Sample	N215-3	B214-15	D113-21	B214-29	B214-08	D217-2
in wt.%						
SiO_2	56.91	66.31	68.37	62.20	68.37	71.90
TiO_2	0.56	0.52	0.51	0.54	0.51	0.49
Al_2O_3	12.13	12.02	11.99	12.07	11.99	11.95
Fe_2O_3*	9.43	7.62	7.22	8.41	7.22	6.54
MnO	0.40	0.41	0.41	0.40	0.41	0.42
MgO	10.65	6.65	5.78	8.40	5.78	4.28
CaO	7.48	4.34	3.65	5.71	3.65	2.47
Na_2O	1.47	0.83	0.70	1.11	0.70	0.46
K_2O	0.58	0.77	0.81	0.69	0.81	0.89
P_2O_5	0.11	0.22	0.24	0.17	0.24	0.28
Total	99.72	99.70	99.70	99.71	99.70	99.69
in ppm						
Cr	683.57	392.22	328.49	519.69	328.49	219.23
Ni	473.54	291.44	251.61	371.11	251.61	183.32
Rb	17.69	27.01	29.06	22.93	29.06	32.55
Ba	181.67	181.42	181.37	181.53	181.37	181.27
Th	3.79	6.56	7.17	5.35	7.17	8.21
U	0.30	0.49	0.53	0.40	0.53	0.60
Nb	4.51	4.74	4.79	4.64	4.79	4.88
Ta	0.76	1.13	1.21	0.97	1.21	1.34
La	16.64	29.42	32.22	23.83	32.22	37.01
Ce	30.57	49.23	53.31	41.07	53.31	60.31
Pr	4.83	7.69	8.32	6.44	8.32	9.39
Nd	20.81	31.24	33.52	26.67	33.52	37.43
Zr	92.20	98.60	100.00	95.80	100.00	102.40
Hf	2.68	2.83	2.86	2.77	2.86	2.92
Sm	4.95	6.55	6.90	5.85	6.90	7.50
Eu	1.19	1.42	1.47	1.32	1.47	1.56
Gd	5.16	6.35	6.61	5.83	6.61	7.05
Tb	0.78	0.91	0.94	0.86	0.94	0.99
Dy	5.01	5.69	5.83	5.39	5.83	6.09
Y	29.11	33.05	33.91	31.33	33.91	35.39
Ho	1.05	1.19	1.22	1.13	1.22	1.27
Er	3.15	3.65	3.76	3.43	3.76	3.94
Tm	0.46	0.52	0.54	0.49	0.54	0.56
Yb	3.07	3.53	3.64	3.33	3.64	3.81
Lu	0.45	0.52	0.53	0.49	0.53	0.56

Table 5. Continued

Metamafic2EA: Epidote amphibolite (D113-5)					
_%metased1	61	67	67	81	56
Sample	B213-7	B214-2G	B214-1	B214-10	B214-16
in wt.%					
SiO_2	66.11	67.81	67.81	71.79	64.68
TiO_2	0.88	0.82	0.82	0.67	0.94
Al_2O_3	13.23	13.02	13.02	12.54	13.40
Fe_2O_3*	7.88	7.52	7.52	6.67	8.18
MnO	0.33	0.35	0.35	0.38	0.32
MgO	3.73	3.47	3.47	2.86	3.95
CaO	5.15	4.47	4.47	2.87	5.73
Na_2O	1.37	1.18	1.18	0.72	1.53
K_2O	0.85	0.88	0.88	0.93	0.84
P_2O_5	0.27	0.28	0.28	0.31	0.26
Total	99.81	99.79	99.79	99.74	99.83
in ppm					
Cr	149.75	135.23	135.23	101.34	161.86
Ni	92.71	90.89	90.89	86.65	94.23
Rb	27.04	28.69	28.69	32.56	25.66
Ba	181.11	181.12	181.12	181.12	181.11
Th	6.04	6.62	6.62	7.95	5.56
U	0.49	0.52	0.52	0.60	0.46
Nb	4.12	4.26	4.26	4.58	4.01
Ta	1.11	1.18	1.18	1.34	1.05
La	28.65	31.04	31.04	36.62	26.65
Ce	47.28	50.90	50.90	59.34	44.27
Pr	7.51	8.04	8.04	9.30	7.06
Nd	30.47	32.44	32.44	37.05	28.82
Zr	99.96	100.89	100.89	103.06	99.18
Hf	2.85	2.87	2.87	2.93	2.83
Sm	6.45	6.75	6.75	7.45	6.20
Eu	1.53	1.55	1.55	1.61	1.51
Gd	6.61	6.78	6.78	7.18	6.47
Tb	0.98	0.99	0.99	1.02	0.97
Dy	6.20	6.24	6.24	6.34	6.16
Y	35.53	35.85	35.85	36.59	35.27
Ho	1.32	1.32	1.32	1.33	1.31
Er	3.99	4.02	4.02	4.11	3.96
Tm	0.58	0.58	0.58	0.59	0.57
Yb	3.90	3.92	3.92	3.99	3.88
Lu	0.55	0.56	0.56	0.58	0.54

1081